Modeling Earth Systems and Environment (2022) 8:5143–5175
https://doi.org/10.1007/s40808-022-01427-1

ORIGINAL ARTICLE

Diagnosing similarities in probabilistic multi-model ensembles: an application to soil–plant-growth-modeling

Aline Schäfer Rodrigues Silva[1] · Tobias K. D. Weber[2] · Sebastian Gayler[2] · Anneli Guthke[1,3] · Marvin Höge[1,4] · Wolfgang Nowak[1] · Thilo Streck[2]

Received: 10 December 2021 / Accepted: 9 May 2022 / Published online: 19 June 2022

Abstract

There has been an increasing interest in using multi-model ensembles over the past decade. While it has been shown that ensembles often outperform individual models, there is still a lack of methods that guide the choice of the ensemble members. Previous studies found that model similarity is crucial for this choice. Therefore, we introduce a method that quantifies similarities between models based on so-called energy statistics. This method can also be used to assess the goodness-of-fit to noisy or deterministic measurements. To guide the interpretation of the results, we combine different visualization techniques, which reveal different insights and thereby support the model development. We demonstrate the proposed workflow on a case study of soil–plant-growth modeling, comparing three models from the Expert-N library. Results show that model similarity and goodness-of-fit vary depending on the quantity of interest. This confirms previous studies that found that "there is no single best model" and hence, combining several models into an ensemble can yield more robust results.

Keywords Multi-model ensembles · Energy statistics · Model set visualization · Crop modeling

Introduction

Multi-model approaches

Multi-model ensembles have received increasing interest in crop-modeling over the last decade (Palosuo et al. 2011; Asseng et al. 2013, 2015; Martre et al. 2015; Wöhling et al. 2015; Yun et al. 2017; Makowski 2017; Wallach et al. 2018). While multi-model approaches can serve different purposes (Höge et al. 2019; Minka 2002), the main focus in the crop-modeling community has been to improve the accuracy of predictions (Asseng et al. 2015; Martre et al. 2015) or to estimate the uncertainty due to model choice, often referred to as conceptual uncertainty (Asseng et al. 2013). Please note that no multi-model method can quantify the conceptual uncertainty on an absolute level (Nearing and Gupta 2018). The reason for this is evident: In practice, there is no way to create and sample from an exhaustive list of all plausible

✉ Aline Schäfer Rodrigues Silva
aline.schaefer@iws.uni-stuttgart.de

Tobias K. D. Weber
tobias.weber@uni-hohenheim.de

Sebastian Gayler
sebastian.gayler@uni-hohenheim.de

Anneli Guthke
anneli.guthke@simtech.uni-stuttgart.de

Marvin Höge
marvin.hoege@eawag.ch

Wolfgang Nowak
wolfgang.nowak@iws.uni-stuttgart.de

Thilo Streck
thilo.streck@uni-hohenheim.de

[1] Department of Stochastic Simulation and Safety Research for Hydrosystems, Institute for Modelling Hydraulic and Environmental Systems/Cluster of Excellence "Data-Integrated Simulation Science", University of Stuttgart, Pfaffenwaldring 5a, 70569 Stuttgart, Germany

[2] Department of Biogeophysics, Institute of Soil Science and Land Evaluation, University of Hohenheim, Emil-Wolff-Straße 27, 70593 Stuttgart, Germany

[3] Junior Research Group for Statistical Model-Data Integration, Cluster of Excellence "Data-Integrated Simulation Science", University of Stuttgart, Pfaffenwaldring 5a, 70569 Stuttgart, Germany

[4] Department of Systems Analysis, Integrated Assessment and Modelling, Eawag-Swiss Federal Institute of Aquatic Science and Technology, Überlandstrasse 133, Dübendorf 8600, Zurich, Switzerland

models that cover the entire range of possible outcomes (Nearing and Gupta 2018; Vehtari and Ojanen 2012; Höge et al. 2019; Ferré 2017).

Therefore, Nearing and Gupta (2018) suggest understanding multi-model methods rather as sensitivity analyses. From this point of view, multi-model methods are tools that make modelers aware of how much predictions may differ within the model set depending on the choice for a certain conceptual model. This follows the line of thought of Ferré (2017) who introduced the idea of a multi-model ensemble as a "team of rivals", which provides competing views of a system. If the competing models agree on a certain prediction, this increases the decision makers' confidence, while disagreement indicates the need for further investigation (Ferré 2017).

When different models are merged to *improve* predictions, modelers hope for two effects that make the ensemble more skillful than its individual members: (1) the errors of the individual models cancel one another. This requires the individual models to be *independent*, i.e. different in their assumptions and conceptualizations (e.g. Abramowitz and Gupta 2008; Abramowitz 2010; Evans et al. 2013; Sanderson et al. 2015a, b; Abramowitz et al. 2018; Enemark et al. 2019). However, this assumption is often not met (Abramowitz and Gupta 2008; Abramowitz 2010; Bishop and Abramowitz 2013; Evans et al. 2013; Sanderson et al. 2015a, b; Knutti et al. 2017; Abramowitz et al. 2018). (2) The ensemble covers a broad spectrum of possible system behavior (Enemark et al. 2019) and thus compensates for over-confident individual models (e.g. Fritsch 2000; Doblas-Reyes et al. 2005; Weigel et al. 2008).

Various studies have compared the predictive performance of multi-model ensembles to the ones of the individual ensemble members (e.g. Krishnamurti et al. 2000; Georgakakos et al. 2004; Doblas-Reyes et al. 2005; Hagedorn et al. 2005; Weigel et al. 2008; Diks and Vrugt 2010; Arsenault et al. 2015; Yun et al. 2017; Christiansen 2018). They found the following aspects to be crucial for the performance of ensemble predictions:

1. the applied combination/averaging/weighting method (Krishnamurti et al. 2000; Doblas-Reyes et al. 2005; Diks and Vrugt 2010; Arsenault et al. 2015; Höge et al. 2019, 2020),
2. the performance measure used for assessing the predictive skills (Hagedorn et al. 2005; Weigel et al. 2008; Diks and Vrugt 2010),
3. the spread (variability) of the individual models (Fritsch 2000; Doblas-Reyes et al. 2005; Weigel et al. 2008), and
4. the similarity of the individual models regarding their structure and their predictions (Tebaldi and Knutti 2007; Abramowitz and Gupta 2008; Abramowitz 2010; Winter and Nychka 2010; Bishop and Abramowitz 2013; Evans et al. 2013; Sanderson et al. 2015a, b; Abramowitz et al. 2018; Enemark et al. 2019).

In the present study, we focus on the last two of these aspects: the similarity and the spread of the individual models. We show how the similarities of (or distances between) the models can be quantified while accounting for the spread in their predictions.

Referring to the often claimed superiority of ensemble predictions, Hagedorn et al. (2005) argue that the question of whether the ensemble has higher predictive skill than the best individual model is posed wrongly because there is often no "best" individual model. They show that it is usually not the same model that performs best considering all quantities of interest or under all conditions. Rather, what is typically identified as the "best" model looking at a particular aspect of the simulated system might be a weak model considering another aspect. Therefore, Hagedorn et al. (2005) conclude that the ensemble is superior to single models because its predictions are more robust, i.e. better over a broad range of predicted variables and modeling periods. We set up the present analysis accordingly, such that it enables a model comparison considering various quantities of interest.

Ensemble predictions in crop modeling

In crop modeling, a systematic assessment of multi-model ensembles was initiated within the Agricultural Model Intercomparison and Improvement Project (AgMIP; Rosenzweig et al. 2013). In the wheat pilot study of that project, Asseng et al. (2013) compared 27 wheat models by analyzing the predicted grain yield under climate change conditions. They found that predictions vary significantly between different models. Thus, there is considerable uncertainty concerning model choice when predicting yields under climate change conditions. In an earlier comparison of yield predictions from eight crop models, Palosuo et al. (2011) also found great differences between the individual models. This study showed that none of the models was able to outperform its competitors across different environmental conditions and for different variables. In addition, the comparison of four crop models by Wöhling et al. (2015) had similar findings that support the argument of Hagedorn et al. (2005) that there is no "single best model".

While Asseng et al. (2013) focused on the "end-of-season variable" grain yield, Martre et al. (2015) compared the same 27 models also regarding grain protein concentration and "in-season variables" (leaf area index, plant-available soil water, total aboveground biomass, total above-ground nitrogen, and nitrogen nutrition index), with all models being calibrated on phenology data. The authors found that the ensemble predictions are more reliable and attributed this improvement to the different process descriptions providing a wide range of plausible system behavior. The study also reports that some models had rather small errors for the end-of-season variables yield and grain protein concentration while showing large errors for in-season variables. Therefore, Martre et al. (2015) emphasize that for comparing the performance of different models, it is important to consider several variables as a model might perform well regarding a certain variable, but poorly regarding others.

Another suggestion of Martre et al. (2015) is to further investigate how to choose the individual models for an ensemble and how to weigh them. Many studies in the climate modeling community found that the dissimilarity of the individual models is crucial for the success of an ensemble (e.g. Tebaldi and Knutti 2007; Abramowitz and Gupta 2008; Abramowitz 2010; Sanderson et al. 2015a, b; Abramowitz et al. 2018). If two models in the ensemble are highly similar, this leads to difficulties in the weighting scheme as these models should not receive the same weight as if they were independent. George (2010) and Garthwaite and Mubwandarikwa (2010) therefore recommend using so-called "dilution priors" that divide the weight between partly redundant models. We hypothesize that quantifying the similarity between the models can help to choose the individual ensemble members and weigh them in a way that accounts for possible redundancies.

Another ubiquitous issue when comparing models is calibration. In a recent study, Wallach et al. (2020) discuss the "chaos in calibrating crop models", i.e. the lack of a unified calibration procedure in the crop modeling community. In an earlier study, Wallach (2011) stated that in the calibration of crop models, often model structural errors are compensated by specifying non-physical parameter values. As a result, a model might perform well for the quantity of interest it has been calibrated on, but poorly for others. This effect is more severe, the more parameters a model has (e.g. Jefferys and Berger 1992; Lever et al. 2016). Therefore, Vogel and Sankarasubramanian (2003) recommend checking model adequacy in an uncalibrated state. We follow that recommendation and implement our analysis in a Monte Carlo framework, sampling prior parameter distributions. This allows us to evaluate the model performance independent of a specific parameter choice and we avoid to cloud model errors by assigning parameter values that compensate for structural deficiencies. As in any Bayesian framework, a subjective choice of prior distributions based on expert knowledge is needed. In fact, in the Bayesian setting, plausible ranges and assumed distributions are part of the model, just as a fixed parameter assumption (or the decision that a parameter is free for calibration) would be part of a model in deterministic modelling. Different choices among these options makeup different models.

Goal and approach of this study

The main goal of this study is to quantify similarities between probabilistic model predictions and visualize them intuitively. The proposed methods help modelers to gain deeper insights into the model set and to choose a suitable multi-model strategy accordingly. Our approach is to use a statistical metric, the so-called energy distance (Rizzo and Székely 2016) to quantify the (dis-)similarity between probabilistic model predictions and noisy measurements. Metrics, in general, are distance measures. Statistical metrics measure how close statistical objects such as probability distributions are, i.e. they take probability densities into account. We use the energy distance as a metric to compare predictive distributions that are generated by sampling from the prior parameter distributions of each model in a Monte Carlo framework. This enables us to take parametric uncertainty into account and to compare the models independent of a specific parameter choice. Thus, for comparing the models, we calculate the energy distance between their predictive distributions.

With the same method, we can also assess model performance by calculating the energy distance between model predictions and noisy observations. For this, we fit a probability density function to replicate measurements. From this distribution, we draw samples to calculate the energy distance in a Monte Carlo framework. If no distribution for the measurement errors can be defined (e.g. because no replicate measurements are available and no assumptions about measurement noise seem defendable), we can use the deterministic counterpart of the energy distance: The so-called energy score (Gneiting and Raftery 2007) compares probabilistic distributions to deterministic values and is directly related to the energy distance. This makes the concept of energy statistics widely applicable for rating probabilistic models.

The proposed method fulfills the following properties:

1. It can act on multivariate model predictions and thus reflect "overall" model characteristics.
2. It quantifies the similarity between pairs of models in the same way as the similarity between models and observations. Thus, it can assess the similarity between model predictions as well as model performance given observed data.
3. It can be used for comparing probabilistic model predictions to both noisy observations (by using the energy distance) and to deterministic observations (by using the energy score).
4. It acts on prior predictive distributions and thus accounts for parametric uncertainty in each model.

For guiding the multi-model process, we need an intuitive way to visualize the quantified similarities among the models and measurements. Therefore, we suggest different methods for visualizing similarities among models, which highlight different aspects of similarity and, when combined, provide a detailed overview for interpreting the model set.

The paper is structured as follows: First, we present the mathematical methods, i.e. the "Energy distance" and the "Energy score", and visualization techniques in the section "Visualizing predictive similarity". Experimental data are presented in "Field experiments" and we introduce the model set in "Model description". This is followed by "Results and discussion". We summarize our findings and provide conclusions in the section "Summary and conclusions".

Methods

Energy distance

In this section, we describe how the (dis-)similarity between two probabilistic models or between a probabilistic model and noisy measurements can be quantified and visualized based on Monte Carlo samples of the models' predictive distributions.

Well-known distance measures like the Euclidean or Manhattan distance (L_P-metrics) are based on the coordinates of points in the Euclidean space. These distances do not take the density of probability distributions into account. In contrast, statistical distances (also known as probability metrics) measure the distance between two statistical objects such as random variables, probability distributions, or data samples (e.g. Deza and Deza 2016) and include information about probability densities.

Rizzo and Székely (2016) introduced the energy distance as a metric that measures the distance between two random vectors X, Y in $\mathbb{R}^D$. It is called energy distance because of the analogy to the potential energy between objects (Rizzo and Székely 2016). It satisfies all axioms of a distance metric (non-negativity, identity of indiscernibles, triangle inequality) (e.g. Deza and Deza 2016). The squared energy distance D^2 between the distributions $F(X)$ and $G(Y)$ is defined as

$$D^2(F,G) = 2\mathbb{E}||X - Y||_2 - \mathbb{E}||X - X'||_2 - \mathbb{E}||Y - Y'||_2 \geq 0, \tag{1}$$

with $\mathbb{E}$ being the expected value, $||\cdot||_2$ being the Euclidean norm, X and X' being independent and identically distributed (iid) variables, the same applies for Y and Y'. In this study, we analyze data based on the energy distance $d(F,G) = \sqrt{D^2(F,G)}$.

The expected values in Eq. 1 can be implemented in a Monte Carlo framework as follows:

$$\mathbb{E}||X - Y||_2 = \frac{1}{N_{\mathrm{MC}}^2}\sum_{k=1}^{N_{\mathrm{MC}}}\sum_{l=1}^{N_{\mathrm{MC}}}\sqrt{\left(\mathbf{x}_k - \mathbf{y}_l\right)^2}, \tag{2}$$

where $x \sim F$, $y \sim G$, and N_{MC} being the number of Monte Carlo samples.

Figure 1 shows four 1D examples that illustrate how the energy distance between two univariate probability density functions (pdf) changes depending on the mean Euclidean distance between these pdfs $\mathbb{E}||X - Y||_2$ and the mean Euclidean distance within each pdf $\mathbb{E}||X - X'||_2$. Analogously, the energy distance can quantify the distance between D-dimensional random vectors.

Comparing Fig. 1a, d as well as (b) and (e) shows that keeping the same mean and increasing the variance of distribution G decreases the energy distance $d(F, G)$ between both distributions. Subfigure (c) shows that for two identical distributions, the energy distance becomes zero, while the expected value of the Euclidean norm $\mathbb{E}||X - Y||_2$ is not equal to 0. Subfigure (f) illustrates the energy distance between two distributions with the same mean but different variances.

Energy score

When working with real and error-prone data, we do not have access to the full distribution of the data (i.e. a "true" value and a distribution function of errors) but only to the measured instances thereof, i.e. our observations. In some cases, these measurements suffice for estimating the underlying distribution reasonably well. If this is not the case (e.g. if there are only a few measurements available), we need an alternative for rating probabilistic predictions given deterministic measurements.

In deterministic modeling, the performance of a model is usually evaluated by an error measure between the model's best estimate $\hat{\mathbf{y}}_k$ and the observations $\mathbf{y}_{\mathrm{meas}}$. Different models are then rated based on the achieved best estimate error, e.g. a root mean square error (RMSE) or the mean absolute error (MAE).

In probabilistic modeling, model rating is based on so-called scoring rules (Gneiting and Raftery 2007). These scores account for the entire predictive distribution of the model instead of only the best estimate. Many different scores exist (Gneiting and Raftery 2007; Yao et al. 2018). Among these, the energy score is directly related to the above-introduced energy distance (Székely and Rizzo 2013), i.e. it resembles the one-sided version of the energy distance (Ziel and Berk 2019). The energy score ES for the model predictive distribution G and observations $\mathbf{y}_{\mathrm{meas}}$ writes as:

$$\mathrm{ES}(G, \mathbf{y}_{\mathrm{meas}}) = \frac{1}{2}\mathbb{E}||Y - Y'||_2^{\beta} - \mathbb{E}||Y - \mathbf{y}_{\mathrm{meas}}||_2^{\beta}, \tag{3}$$

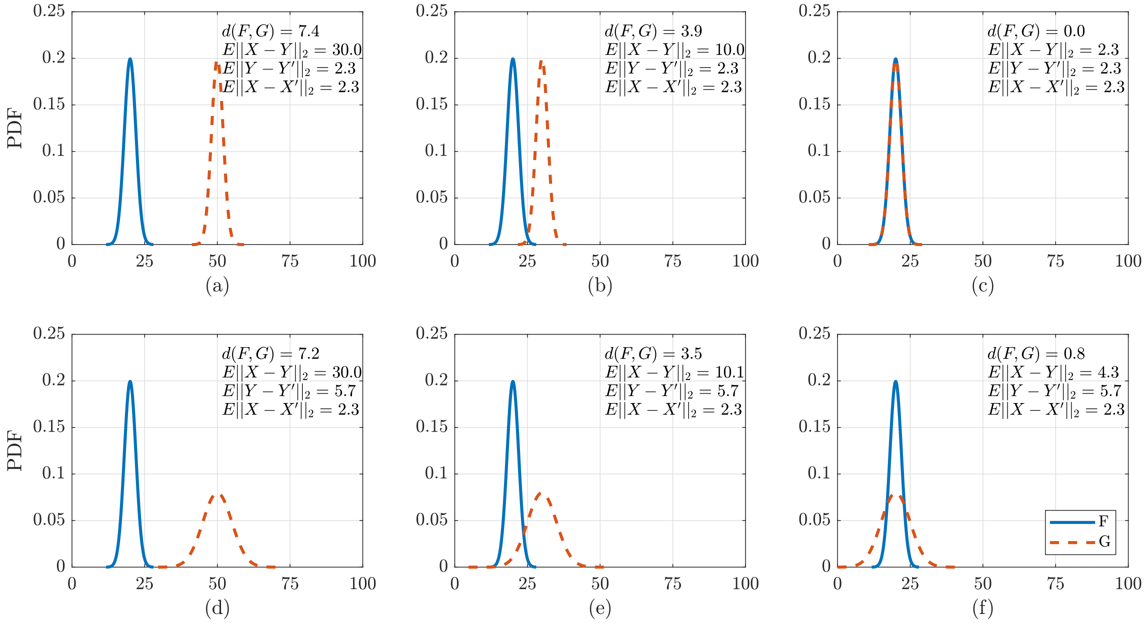

Fig. 1 Illustrative 1D example of the energy distance $d(F, G)$ between two probability density functions F and G. It is calculated based on the mean Euclidean distance between these functions $\mathbb{E}||X - Y||_2$ and the mean Euclidean distance within each function $\mathbb{E}||X - X'||_2$ and $\mathbb{E}||Y - Y'||_2$, respectively

with $\beta \in (0, 2)$. We choose $\beta = 1$ as it is a standard choice for distributions that are not heavily tailed (Ziel and Berk 2019). For $\beta = 2$, the energy score is equal to the negative squared error (Gneiting and Raftery 2007).

In cases we cannot assume a reasonable distribution based on replicate measurements, we will use the energy score instead of energy distance. We want both quantities to act on the same scale, so they are directly comparable. Therefore, we use $d(F, G) = \sqrt{D^2(F, G)}$ and $\sqrt{\text{ES}}$ for the analysis.

Visualizing predictive similarity

We want to visualize the (dis-)similarity of the model predictions to get an intuitive understanding of the diversity in the considered model set. At the same time, we want to visualize how well the predictions match the measurements. Therefore, we treat both the models and the measurements as objects in a common model predictions-observations space, which we call "quantity of interest space". Representing the similarities of N objects (models and observed data) leads to $n_{\text{comb}} = N \cdot (N - 1)/2$ combinations. While in our application, this number (three models and one measurement data set, hence, six combinations) is comparatively small, visualization of model similarity in two dimensions is already not a straightforward task. Clearly, the number of models to be compared can become much higher in extensive multimodel ensembles. Therefore, the methods we propose for visualization are also suitable for larger model sets.

Each of these objects (models and observed data) consists of n_{qoi} variables (quantities of interest). In the case of probabilistic modeling, each variable is assigned a probability distribution. Therefore, we have to deal with high-dimensional data, and regarding its two-dimensional visualization, we have to balance the interpretability and the preservation of the original structure in the applied projection (Liu et al. 2017), which is a typical problem in the visualization of high-dimensional data.

We make use of different techniques for visualizing the similarity of two objects (model-model, model-data) under different conditions. Each visualization method highlights a different aspect, so which method is the most insightful one depends on the specific question we ask about the model set:

1. Heatmaps: In a matrix, the distances between all pairs of objects are visualized through varying colors or intensity (e.g. Nandi and Sharma 2020).
2. Radar charts: Several axes are arranged radially starting from a common center. Each axis represents a certain quantity of interest, i.e. a different variable or the same variable under different boundary conditions. Each value (here, the distance between two objects) is plotted along one axis. This is repeated for all axes. Finally, all values are connected to a polygon, representing one object (e.g. Nandi and Sharma 2020).
3. Dendrograms: Dendrograms are tree-like diagrams that are typically used for visualizing hierarchical structures. A dendrogram consists of branches that connect objects

depending on their similarity. The height at which two objects are joined together represents the distance between these objects (e.g. Nandi and Sharma 2020). For creating such a diagram, we use an agglomerative hierarchical clustering approach (Xu and Wunsch 2008): An algorithm identifies pairs of clusters with minimal distance in-between and merges them. This merging procedure is repeated until all data points are finally in one overarching group (Xu and Wunsch 2008). The merging depends on the chosen linkage method, i.e. the definition of the distance between two clusters. For the present study, we chose a linkage that uses the average distance between data points in two clusters.

Case study description

Central to our study is the simulation of wheat growth, energy and water fluxes in six agricultural fields in two regions during several years (2010–2015). These fields feature slightly contrasting meteorological conditions at two different sets of sites (1–3 and 4–6), with soils being only similar in sites 1–3. The study is based on an extensive data set enabling coupled soil–plant-growth modeling and comparing simulation results to high-quality measurements. The field data is summarized in “Field experiments” and the participating models of the ensemble in “Model description”.

Field experiments

The data set used in this study is a subset of a multi-site, multi-year, and multi-crop data set that contains extensive characterization of soil properties and states, plant growth and yield, management, and soil–atmosphere fluxes of energy, water and carbon dioxide. It was obtained from measurement campaigns in intensively managed agricultural fields of local farmers. We will limit the description of the data set to a minimum since it was published alongside a manuscript with full methodological details (Weber et al. 2021).

The data were collected between May 2009 and September 2018. In this study, we use a subset that covers the sites and years in which winter wheat was cultivated from 2010–2015 (year of harvest). The combination of a site at which and a year during which winter wheat was cultivated are reported as site-years. For example, winter wheat grown at site 1 from November 2014 to July 2015 is denoted as site 1, year 2015. In total, we analyze data of 14 site-years. Details of the two regions can be found in Weber et al. (2021), and their soil properties are summarized in Table 1.

All required meteorological forcings were measured at half-hourly time intervals and data gaps were filled. In the data set, grain yield was reported both by the farmer as a field average and by extrapolation of the plot sampling to the field. Phenology and leaf area index were measured at least biweekly during the main vegetation season (April to mid July).

Table 1 Properties of the soil horizons at sites 1–6, and the soil hydraulic property model parameters θ_s and θ_r, which are the fixed saturated and residual water content, respectively

Site	Depth	No. of simulation layers	Organic matter	Clay	Silt	Sand	Bulk density	θ_r	θ_s
(–)	(cm)	(–)	($gg^{-1} \cdot 100$)				($g\,cm^{-3}$)	($cm^3\,cm^{-3} \cdot 100$)	
1	0–30	6	1.75	18.2	79.4	2.5	1.37	7.5	46.0
	30–45	3	0.61	18.8	79.2	2.0	1.51	7.2	42.9
	45–165	24	0.42	18.7	80.4	0.9	1.48	7.3	43.9
2	0–30	6	1.53	17.9	79.5	2.6	1.33	7.6	47.0
	30–45	3	0.52	20.1	77.0	2.9	1.46	7.5	43.9
	45–165	24	0.34	18.7	79.7	1.6	1.53	7.1	42.5
3	0–30	6	1.64	17.1	81.1	1.8	1.37	7.4	46.2
	30–45	3	0.83	18.7	80.4	1.0	1.50	7.3	43.4
	45–165	24	0.63	16.1	83.0	0.8	1.51	6.9	43.2
4	0–20	4	4.35	37.8	56.0	6.2	1.31	9.5	49.2
	20–30	2	2.13	38.6	52.5	8.9	1.34	9.4	48.2
	30–50	4	1.63	48.4	43.3	8.4	1.32	10.0	50.0
5	0–20	4	3.64	28.9	68.3	2.8	1.37	8.6	46.8
	20–60	8	1.44	33.6	64.3	2.1	1.40	8.9	46.7
	60–165	21	0.71	34.2	64.0	1.8	1.51	8.7	44.0
6	0–30	6	5.50	45.6	51.2	3.2	1.04	10.7	59.0
	30–45	3	3.88	47.6	48.3	4.1	1.29	10.1	51.3

Model description

The relevant processes for crop development and growth, unsaturated water flow, nitrogen and carbon turnover in the soil, evapotranspiration, and drainage water quantity and quality were simulated with the multi-model library Expert-N (Priesack 2006). Expert-N is a model system that facilitates a high degree of flexibility in selecting competing model formulations for the relevant processes in the soil-vegetation-atmosphere continuum. An example of a 48 member multi-model ensemble using Expert-N is the study about climate change impact on wheat and maize yield development in Ethiopia by Rettie et al. (2022). That study uses a model ensemble consisting of 48 unique model members set up in Expert-N. For the presented study we selected three different plant growth models within Expert-N: CERES (Ritchie et al. 1988), SUCROS (van Laar et al. 1997), and SPASS (Wang and Engel 2000; Gayler et al. 2002), which are coupled to the soil carbon and nitrogen turnover and transport models SOILN (Johnsson et al. 1987) and LEACHN (Hutson and Wagenet 1995), and the Richardson–Richards equation for variably saturated water flow as implemented in HYDRUS-1D (Šmunek et al. 1998). Fluxes of heat and dissolved nitrogen in the soil were described by LEACHN and potential evapotranspiration as calculated by the Penman–Monteith equation (Allen 1998) modulated by crop coefficients. These models are described in “Phenological development”– “Soil nitrogen”. The model initial and boundary conditions, including a description of the uniformly distributed and bounded model parameter priors for sampling the prior predictive distribution, are given in “Process models”. In the following, SUCROS, CERES, and SPASS are described and refer to the versions implemented in Expert-N v.3.1. Model parameters and priors are listed in Tables 5, 6, and 7.

Phenological development

In Expert-N, the phenological development (BBCH) is modeled as a parametric function of thermal time, vernalization, photoperiod effect, and temperature sensitivity. While CERES is differentiated into nine development phases, SPASS and SUCROS are differentiated into three. All three adopted models distinguish the vegetative growth phase (BBCH $\leq$ 60) from the generative phase (BBCH $>$ 60) and one for emergence. CERES (Ritchie and Godwin 1989; Jones 1986) and SUCROS (Spitters et al. 1989; Van Laar et al. 1992) are widely established models and SPASS is a combination and development out of the other two (Wang 1997; Gayler et al. 2002). Internally, phenological development is first simulated as a development stage on a scale from $-$ 0.5 to 2.0, and is subsequently converted to an externally reported BBCH variable using fixed lookup tables with 10 support points (11 in the case for SPASS). The support points in the lookup tables were considered as fixed. The simulated phenology acts as a boundary condition for the remaining part of the dynamic plant growth model, by setting the precondition after which certain other parts of the model are active (i.e. triggering submodules for, e.g. leaf area index or grain filling after anthesis at BBCH = 60). An important difference between the models is that winter wheat requires vernalization, which is the induction of flowering after a cold period. In contrast to CERES and SPASS, which contain routines for vernalization. Since SUCROS does not include vernalization, it is strictly speaking, a spring wheat model.

Root growth, root water uptake, and transpiration

Dynamic root growth in all plant models is simulated by roots growing downward up to a maximum root extension depth. The maximum growth rate is reached under optimum conditions. This is modulated by impacts of unfavorable environmental factors (temperature, soil moisture) in the layer of the currently greatest root extension. Specifically, these impedances are functions of temperature and low soil moisture (SPASS, SUCROS), or of low soil moisture and low mineral nitrogen contents (CERES). In each simulation layer, the active roots are the balance between root growth and senescence at each time step (Gayler et al. 2013). To calculate root water uptake, a root length density is required. CERES and SPASS use an identical approach: the root length growth rate is linearly related to the root biomass growth rate, and the vertical distribution is related to water and nitrogen availability in the respective soil layers. In SUCROS, the root length growth rate is derived for each simulation layer based on a crop-specific root depth distribution function, the root biomass, and a specific root length. The upper limit of root water uptake is limited to the potential transpiration as calculated by the Penman–Monteith equation (Allen 1998). In the case of SPASS and CERES, a maximum root water uptake rate per root length is additionally defined. All three models use a macroscopic approach in which root water extraction is distributed to the individual simulation layers proportionally to the relative root length in the layers, as long as the water supply is optimum. Impedance factors such as oxygen deficiency in (near-)saturated soils, soil compaction and structure, disease and pests, adverse chemical conditions (e.g. salts) are not considered in the models. To account for crop effects on potential evapotranspiration, all three models use crop coefficients, which we modeled as a piece-wise phenology-state dependent function with three parameters kc_{ini} (−), kc_{mid} (−), and kc_{end} (−), which are the crop coefficient for the initial, mid and end of the vegetation period, respectively. These parameters were considered uncertain with the uniform distribution in the ranges given in the Appendix, Table 4.

CO_2 assimilation, biomass growth and leaf area development

CERES adopts a robust "big leaf" approach to calculate carbon assimilation, using empirical adjustments to account for the depth-dependence of photosynthetic capacity and light response, with the interception of photosynthetically active radiation dependent on leaf area index. Biomass development depends on the partitioning of assimilates to different plant organs (roots, leaves, stem, and fruit). It is achieved through potential growth rates and a priority scheme for the allocation of assimilates to each organ (differentiated into five developmental stadia). In the juvenile phase, i.e. in the stadium between the emergence and, the development of the first apical spikelet, the leaf area index develops exponentially, and after the juvenile phase, leaf area develops proportionally to the leaf biomass development, depending on temperature, and water and nitrogen stress. In SUCROS and SPASS, the calculation of carbon assimilation is based on a multi-layer approach, which is more comprehensive compared to CERES. The aim of this approach is to differentiate between sunlit and shaded leaves and to account for the attenuation of direct and diffuse radiation. The two models differ in vertical resolution as SUCROS uses a three-layer approach, and SPASS uses five layers, but the calculation of leaf internal CO2 concentration and net photosynthesis is similar, with small differences in the calculation of water stress and nitrogen response functions. In contrast to CERES, in SPASS and SUCROS carbohydrate allocation and hence organ growth follows an assimilate-partitioning scheme, which is fixed at optimum water supply and is determined solely by the development stage of the plant. However, in the case of water deficiency, root growth is favored in both models to counteract the cause of stress. In SUCROS, the leaf area growth is directly coupled to leaf biomass growth rate, whereas in SPASS, leaf area growth rate does account for water and nitrogen deficiency. More detailed presentations can be found in Priesack (2006), Priesack and Gayler (2009), Biernath et al. (2011), Wöhling et al. (2013) and references therein.

Soil hydrology

In Expert-N, the standard process model for simulating variably saturated moisture fluxes in soils is the Richardson–Richards equation (RRE) (Richardson 1922; Richards 1931). The solution of the RRE requires parameter functions to describe the soil hydraulic properties. Since we simulated root water uptake using a macroscopic approach (van Dam et al. 2008), it is sufficient to parameterize the RRE using the van Genuchten Mualem model (van Genuchten 1980). There would be physically more comprehensive soil hydraulic property models that account for water storage and conductivity in medium to dry soils (Weber et al. 2019; Streck and Weber 2020; Weber et al. 2020). These would influence the simulation of actual transpiration under water-stressed conditions only when using microscopic (not macroscopic) root water uptake models (van Dam et al. 2008), providing hydraulic uplift does not influence the simulation.

For each site, a top-soil/sub-soil differentiation was made, each with a different parameterization. The varied parameters per soil layer are α (cm^{-1}) and n (–), which are the van Genuchten shape parameters, the saturated hydraulic conductivity K_s ($\mathrm{cm\,d}^{-1}$), and the tortuosity parameter τ (–), and we fixed $m = 1 - 1/n$. Instead of varying the saturated and residual water contents, $\theta_r(-)$ and θ_s, respectively, we vary the soil water content profile set as an initial condition. The soil model is discretized into simulation layers of 5 cm depth (see Appendix, Table 1). Here, in contrast to the observed soil profiles, we reduce the number of simulated soil horizons for the soil hydrological part to two by merging the second and third horizon at sites 1–5. The differentiation into more horizons is pedologically founded, but for the modeling purpose of this study not parsimonious, i.e. we group horizons with very similar hydraulic properties.

Soil nitrogen

Mineralization, nitrification, and denitrification are modeled following the SOILN approach, while urea hydrolysis, volatilization and dissolved nitrogen transport are modeled using the LEACHN approach.

The model concept of SOILN differentiates three pools of organic nitrogen representing the three different pools of organic carbon, available to the soil microbes. These pools are termed 'litter', 'humus', and 'manure'. The 'litter' pool, a pool with fast turnover rates, represents fresh organic matter and microbial biomass. The 'humus' pool with a slow turnover of soil organic carbon, and the 'manure' pool, which represents the organic fertilizer. There are two essential assumptions of this model concept; (i) the N demand for the internal carbon cycle is governed by a constant C/N ratio of 10:1 in the microbial biomass and in the humus pool, and (ii) mineral nitrogen that is released or assimilated by the microbial biomass, follows this ratio. We varied the rate constants $k_{\mathrm{miner,man}}$ (d^{-1}), $k_{\mathrm{miner,lit}}$ (d^{-1}), $k_{\mathrm{miner,hum}}$ (d^{-1}), which govern the rate of mineralization of the manure, litter, and humus pools. We also varied the rate coefficients for the nitrification k_{nit} (d^{-1}) and denitrification $k_{\mathrm{miner,lit}}$ (d^{-1}), where, analogously to the treatment of the soil hydraulic properties, we model the two horizons with different sets of kinetic rate constant parameters, except for $k_{\mathrm{miner,man}}$, which we set to 0 for the sub-soil. The rate constant for the urea hydrolysis $k_{\mathrm{urea,hy}}$ is a constant 0.36 (d^{-1}). The effectivity of decomposition f_{e} (–) describes the fraction of carbon that is re-immobilised after decomposition and set to a constant 0.45. The humus development constant f_{h} (–) describes the fraction of decomposed litter that is added to the humus pool and was set to 0.2.

Model setup and implementation

Process models

As an upper boundary, we generally use in situ measured daily aggregated atmospheric temperatures (minimum, mean, and maximum), global radiation, wind speed, and precipitation. Potential evapotranspiration fluxes were calculated based on the Penman–Monteith approach. For the solutes, we use flux boundary conditions prescribing constant atmospheric NH4 deposition, and the timing, frequency, type, and amount of fertilizers. At the lower boundary, we used free drainage for the water flow module and a zero gradient for the solute and heat flux modules. Field management in terms of nitrogen input by fertilizers, and sowing and harvest dates were set to the farmer-reported data.

The selection of which parameters are considered as uncertain priors, and their respective ranges and distributional assumptions was guided by both model system and expert knowledge. Details are listed in Tables 4, 5, 6 and 7). We ran simulations based on n_{MC} = 10,000 parameter vector realizations generated by Latin Hypercube sampling per site-year and model. The gained forward simulation results resemble approximations to the prior predictive distributions for each of the 14 site-years and each of the plant models. This resulted in a total of 420, 000 individual simulations performed on the High-performance Cluster bwFOR of the Federal State of Baden-Württemberg. The varied model parameters are listed in the Appendix in Tables 4, 5, 6 and 7.

Similarity analysis

We analyze the similarity of probabilistic predictions of CERES, SUCROS, and SPASS (Priesack 2006) via the energy distance between the predictive distributions of the models for different variables. The analyzed variables are yield, phenology, and leaf area index. For comparing model predictions and measurements, we use either the energy distance or the energy score as discussed in "Energy distance" and "Energy score":

1. *Fitting a distribution to the observations and using the energy distance:* In the case of yield predictions, we can reasonably assume a Gaussian measurement error and, hence, define a distribution for the observations. Therefore, we can use the *energy distance* not only for the pairwise comparison of the models' distributions among each other but also for the comparison with the distribution fitted to the observations.
2. *Using the median of the observations and the energy score*: In the case of the other two variables, leaf area index and phenology, making assumptions about measurement error and fitting a distribution to the observations is not as straightforward. Instead, we take the median of the measurements and use the *energy score* to compare the models and the observations. For the comparison of the models among each other, however, we still use the *energy distance* because the predictive distributions are available.

Please remember that similarities quantified by the energy score and the energy distance are on the same scale, and hence directly comparable.

We analyze data from six sites and up to three years per site to check how model performance and similarity vary under different conditions.

Results and discussion

First, we compare the models' similarity (among each other) and their performance (i.e. similarity to observations) based on the end-of-season variable yield. Later, we analyze in-season variables to gain more insight into the processes that may have led to differences in the final yield predictions.

Analysis of the end-of-season variable yield

For yield, we assume a Gaussian measurement error, describing the distributions based on the replicates' mean and variance. The resulting distributions are shown in Figs. 2 and 3. Based on Monte Carlo samples of these distributions, we calculate the energy distance between models and observations.

Predictive distributions

Figures 2 and 3 depict the distributions for yield predicted by the three models and the measurements for the sites 1–3 and 4–6, respectively. The probability density functions represent the prior model predictions, i.e. the models have not been calibrated and represent the full range of plausible parameters as defined in Tables 5, 6 and 7.

The mean observed values for yield range from 7.0 t/ha (site 2, 2013) to 9.2 t/ha (site 4, 2014), the corresponding standard deviations range from 0.39 t/ha ≈ 5% (site 2, year 2011) to 2.1 t/ha ≈ 23% (site 6, year 2014).

The probability density functions show that the predictions made by SPASS (yellow) have the highest variance for

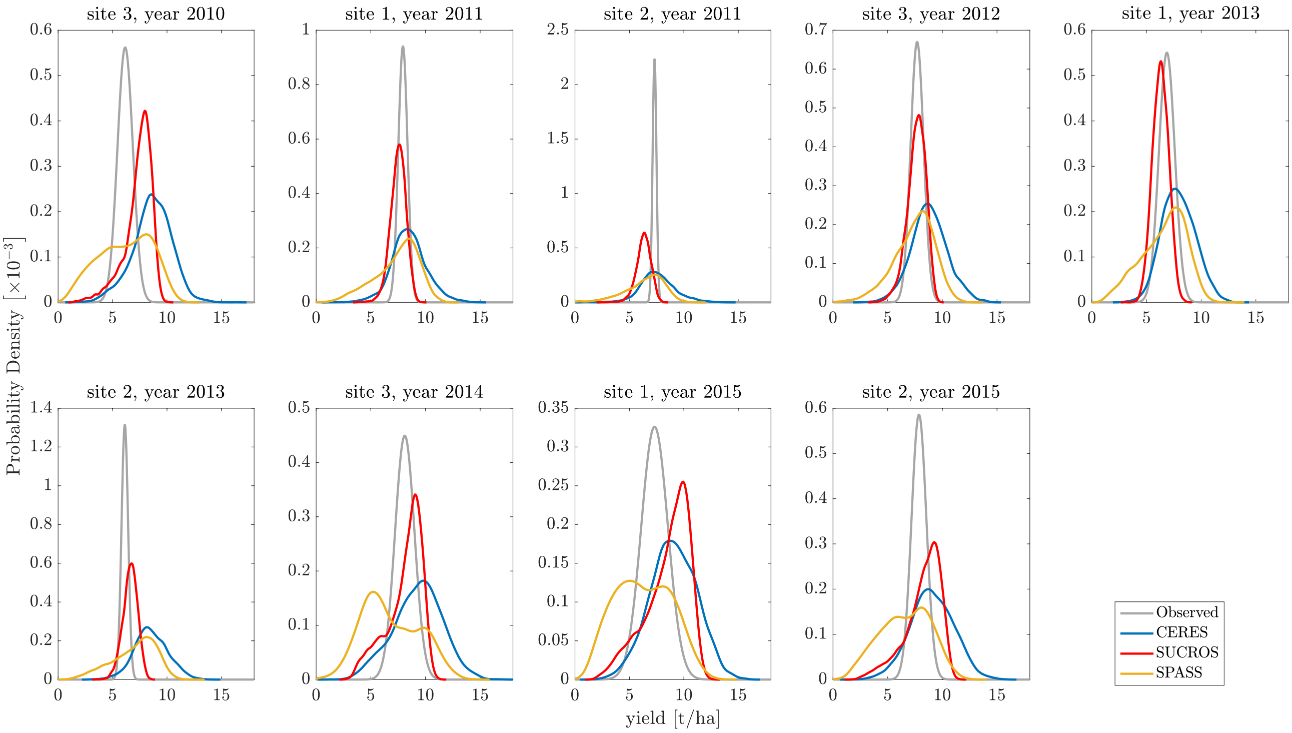

Fig. 2 Probability density functions of the yield predicted by the three models and observed (gray), sites 1–3. For better visualization, *y*-axis scales are not the same across all sub-plots

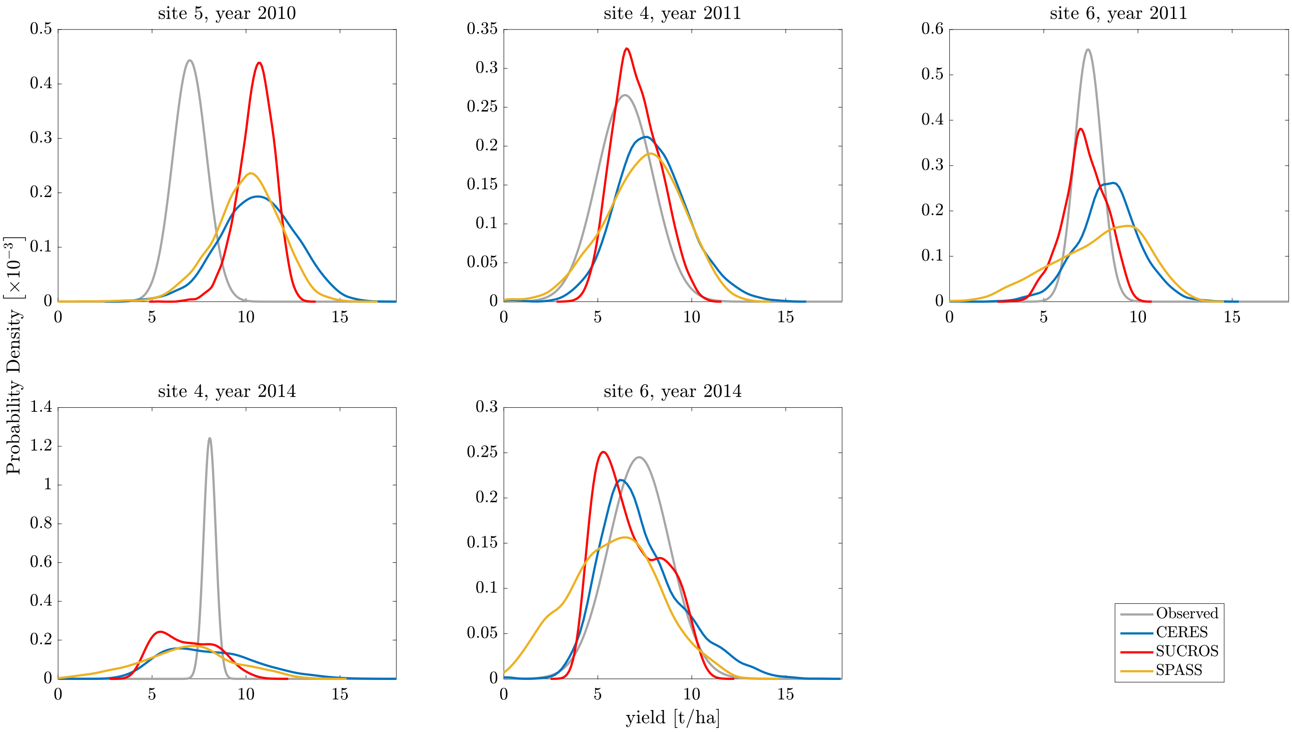

Fig. 3 Probability density functions of the yield predicted by the three models and observed (gray), sites 4–6. For better visualization, *y*-axis scales are not the same across all sub-plots

all sites and years and it predicts ranges of very low yield with a higher probability than CERES (blue) and SUCROS (red) do. For most cases, SUCROS shows the smallest variance in the yield predictions and, from the visual impression, the best goodness-of-fit to the measurements (gray).

Energy distance-based similarity analysis

To get a more aggregated and objective comparison of the predictive distributions of all models and the data, we quantify their similarity according to their prior predictive distributions using the energy distance (Eq. 1). In the following, we discuss corresponding visualizations with radar charts, dendrograms, and heat maps.

Visualizing model similarities using radar charts

Figure 4 shows four radar diagrams that represent the similarity of the models and the observations, each centered on one of the models, or the observations, respectively. In each chart, each model is represented by points that are connected across all radial axes. Each axis represents one site-year. The closer a point to the center, the lower the energy distance between the respective distributions, i.e. the more similar the distributions.

The background color of each segment is color-coded according to the weather conditions of the respective site-year. For this color-coding, we calculated the ratio of mean precipitation and mean temperature from April to June p/T and represent low values as red and high values as blue. This color-code is useful to investigate if there is any obvious relationship between weather conditions and model performance or similarity.

From Fig. 4a we can see that SUCROS is closest to the observed data for most site-years. In parts, this can be explained by SUCROS showing the lowest variance in the yield predictions, while being reasonably centered on the observations (see Figs. 2, 3).

Comparing model performances for sites 1 and 2 in 2013, we notice that CERES and SPASS are much closer to the data for site 1 than they are for site 2. Considering that the conditions at both sites are very similar, it may be surprising that the models perform so differently. The model predictions for both sites are indeed highly similar. However, the observations' variances differ considerably between both sites (see Fig. 2). Please recall the property of the energy distance that decreasing the variance of a distribution while keeping the same mean increases the energy distance between two distributions (see Fig. 1). This effect is clearly visible in the case of model performances for site 1 and 2 in 2013.

Focusing on the weather conditions during the growing season, we see that all models perform relatively poorly for site 5, 2010, which was a rather wet year at this site. Here, SPASS is slightly closer to the measurements than the other two models. This is due to the high variance of its predictions (see Fig. 2), which leads to a larger overlap of the predictive distribution with the measurement distribution, even though the modes of all three predictive model distributions are relatively similar, all overestimating the yield. For the other wet year 2013, we cannot observe a similarly poor performance of all models. Only the CERES predictions of site 2, 2013 show a rather high distance to the observations again overestimating the measured yield (see Fig. 2). However, for the relatively dry conditions at site 3 in 2010, CERES shows a similar distance as it again overestimates yield (see Fig. 2). Hence, in the current data set, the poor performance of the models cannot be clearly explained by specific weather conditions.

Next, we check whether any of the models perform above its average during certain weather conditions: CERES performs well for site 6 in 2014, which was a rather dry year. SUCROS shows equally good performance under both dry and wet years. SPASS performs comparatively well for site 4 in 2011, which was the second driest year in our data set. However, this is not true for other dry years in this data set.

In summary, we cannot observe a specific pattern of good or poor model performance under certain weather conditions. This result indicates that the data do not provide evidence for identifying systematic mispredictions based on climate or site. An exception is site 5, which, however, only has one replicate year, so that no general statement can be made.

In Fig. 4b–d, we focus on the similarity between the models. When CERES is in the center of the radar chart (subfigure (b)), we can see the high discrepancy between CERES and SPASS for site 3, 2014, site 1 and 2, 2015, site 3, 2010 (rather dry years). The highest distance between CERES and SUCROS occurs for site 1 and 2, 2013 (wet years). When SUCROS is centered (subfigure (c)), it is apparent that SPASS is closer, i.e. more similar for most site-years. Subfigure (d), with SPASS being centered does not contain new information that has not yet been shown in figures (a)–(c) and is only shown for the sake of completeness.

Visualizing model similarities using dendrograms

In Fig. 5, an alternative visualization of model similarities based on dendrograms is presented. Here, the data of sites 1–3 are shown, the corresponding Figure for sites 4–6 can be found in the appendix (Fig. 11). Please note that the order of the models is not necessarily the same for all dendrograms. Rather, this so-called leaf order was optimized such that the sum of the similarities between adjacent leaves is maximized (Novoselova et al. 2015).

From the way models and observations are merged into clusters and from the height at which two objects are joined together in the dendrograms, we can intuitively see their similarity.

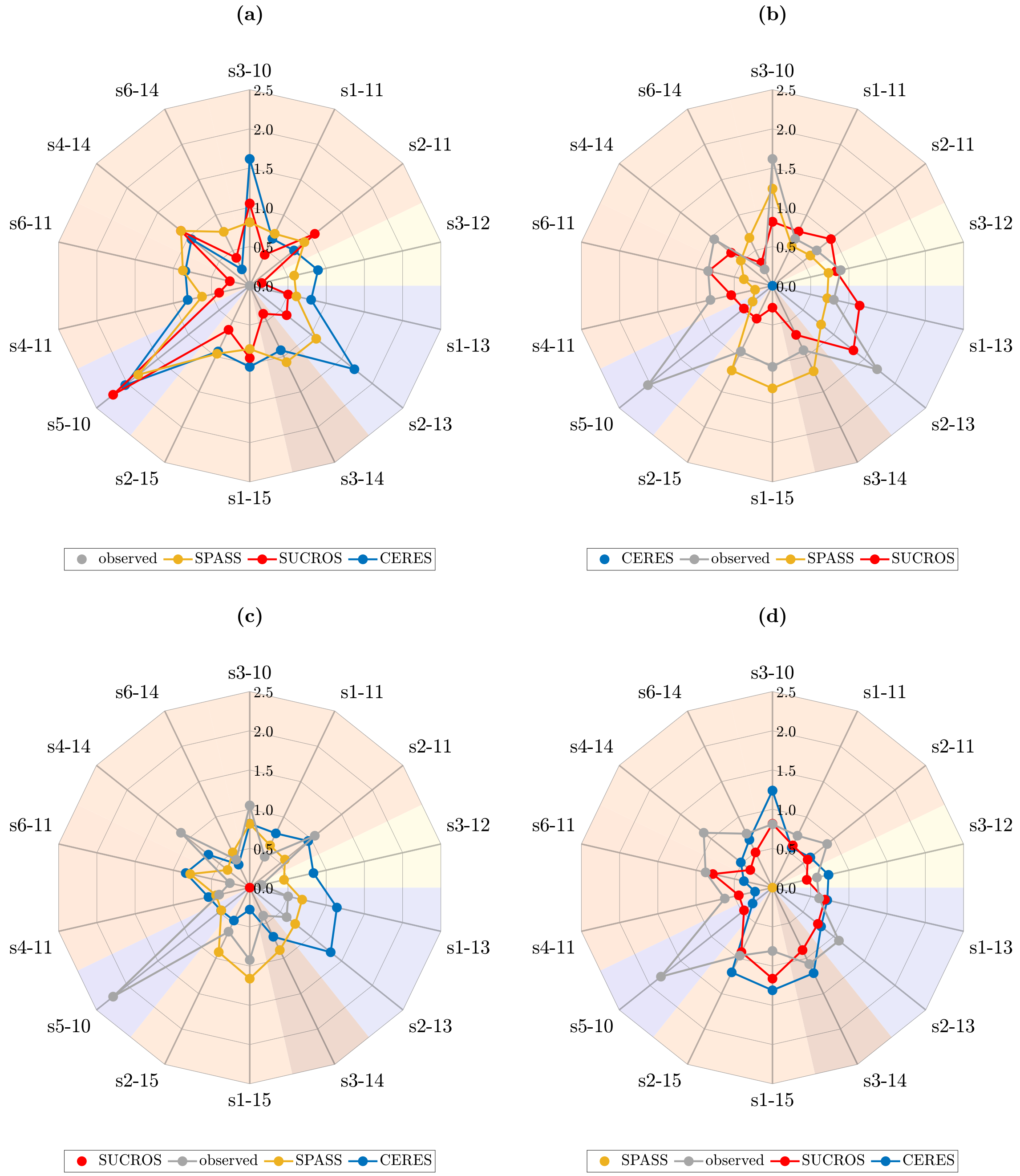

Fig. 4 Radar charts showing the energy distance between all models and observations based on yield predictions. In each subplot, one of the models or the observations are centered. Each colored line represents the distance of one model or the observations to the data set in the center. Each axis represents one site-year (abbreviated as, e.g. "s1–11" for site 1, year 2011). Segment colors resemble the annual weather conditions: hot and dry (red), average (yellow) to cold and wet (blue)

As can be seen from Figs. 5 and 11, different clusters are formed for different site-years. This shows that both, model similarity and goodness-of-fit, vary depending on the site-years.

Visualizing model similarities using heatmaps

In the heatmaps shown in Figs. 6 and 12, small values are represented by light colors and large values by dark colors. To dissect the individual components that the energy distance consists of, we plot its constituent parts $\mathbb{E}||X - Y||_2$ and $\mathbb{E}||X - X'||_2$ separately. The main diagonal entries represent the spread within the predictive distribution of a single model $\mathbb{E}||X - X'||_2$, while the off-diagonal entries represent the similarity of two objects $\mathbb{E}||X - Y||_2$.

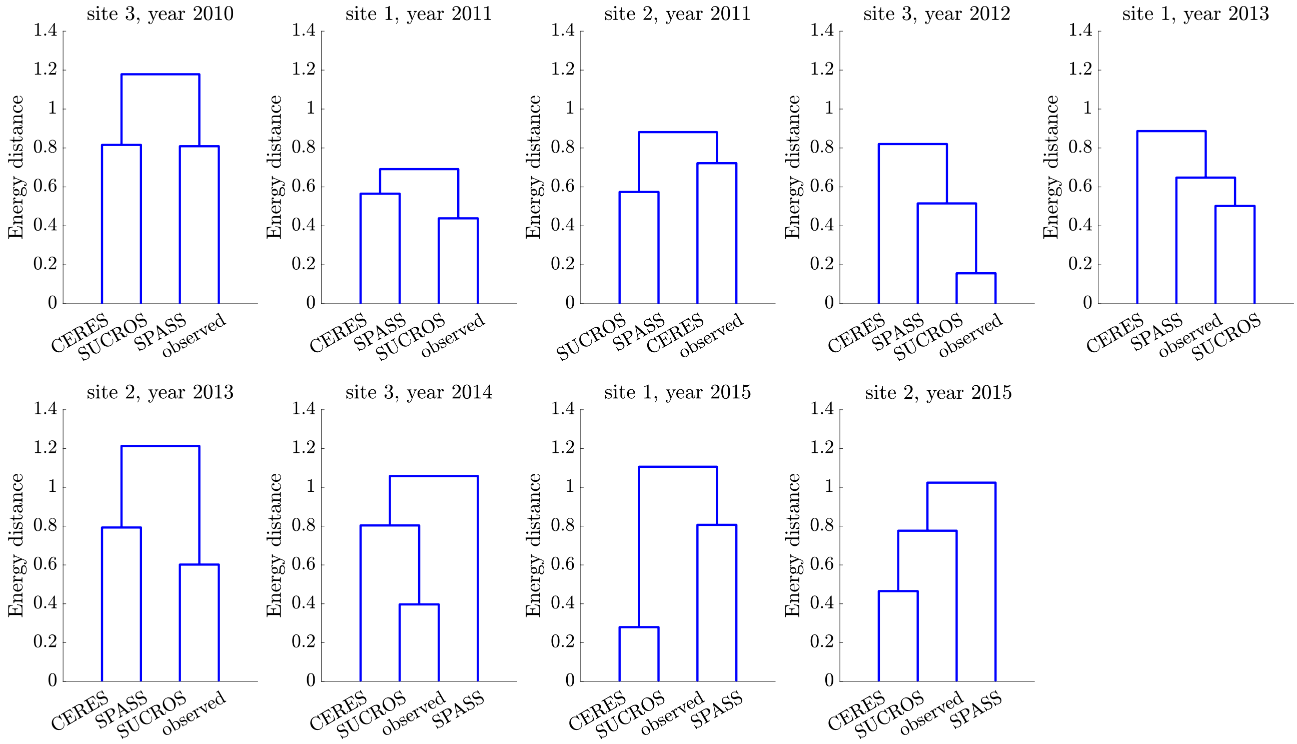

Fig. 5 Dendrograms showing the energy distance between models and observations based on yield predictions, sites 1-3

From the color-coding, we can intuitively see that the highest dissimilarity among the models occurs for site 3 in 2010 and 2014, as well as for sites 1 and 2 in 2015, as these heatmaps are overall darker than the others. In the same manner, it is immediately obvious that SPASS clearly differs from the other models and the measurements. This is neither visible in Fig. 4 (radar charts), nor in Fig. 5 (dendrograms). The last columns/rows show the goodness-of-fit to the observations. Here, it is clearly visible that SUCROS performs best and SPASS performs worst for most site-years.

Comparison of the visualization methods

Table 2 summarizes the properties of the three visualization methods and their applicability for different use cases.

With heatmaps and dendrograms, all objects (here: models) can be compared at one glance, however, only for one condition (here: site-year). Therefore, for comparing many models under specific conditions (e.g. per site-year), heat maps and dendrograms are suitable. In contrast, radar charts are useful for comparing one object (e.g. measurement data) to a small number of other objects (e.g. models) under many different conditions (e.g. site-years).

Dendrograms make it easy to identify clusters. Such clusters can, for example, indicate settings in which all models are similar, but are far from measurements. Such a case may point to the fact that an important process was not considered in any of the models. Examples for such a setting are the yield predictions for site 5, year 2010 and site 4, year 2014 (see Appendix B1). Of course, we can also see from the density functions in Fig. 3 or the radar chart centered on the observations (Fig. 4) that none of the models fits the measurements for this site-year well. However, the analysis based on density functions is only trivial in 1D cases such as the exemplary yield predictions used here. Imagine if we wanted to compare higher dimensional predictions. In such cases, this task would be much easier using dendrograms based on probability metrics. Also the analysis based on radar charts would be less convenient for identifying clusters: we can tell from the radar chart centered on the observations that all models are far off. However, we cannot tell based on the same radar chart whether the models are close to each other. To get this insight, we would have to analyze several radar charts with different models being centered.

Summary regarding the Expert-N model set

Summarizing the comparison of the Expert-N model set, SUCROS performs best in predicting yield based on the similarity of its prior predictive distribution and the distribution of the observations. The highest similarity among the models is between SPASS and SUCROS, while the biggest differences appear for SPASS and CERES. Our analysis confirms that yield predictions vary significantly between different models as Asseng et al. (2013) and Palosuo et al. (2011) found in earlier studies.

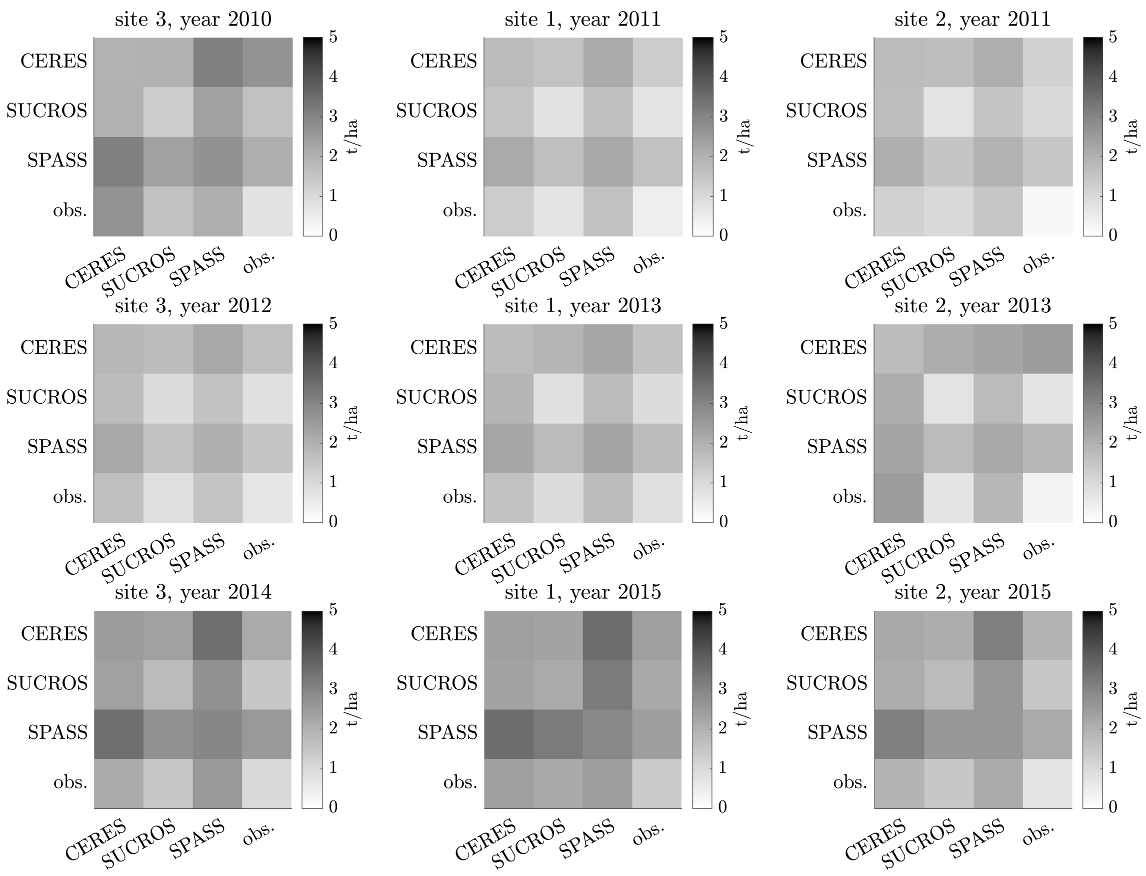

Fig. 6 Heatmaps reflecting the similarities between models and observations based on yield predictions, for sites 1–3. The color-coding represents the values of the individual components of the energy distance: $\mathbb{E}||X - Y||_2$ (off-diagonal entries) and $\mathbb{E}||X - X'||_2$ (main diagonal entries)

Table 2 Comparison of the visualization methods

Visualization method	Radar charts	Heat maps	Dendrograms
Type	Axis-based	Matrix-based	Hierarchy-based
Comparison of many objects	×	✓	✓
Comparison of many conditions	✓	(✓)	×
Easy identification of clusters	×	(✓)	✓
Color-coding possible	✓	(✓)	(✓)
Variation within and between objects	×	✓	×

The checkmark means that the method is well suited, the checkmark in parentheses means that the method can be used for the task in certain cases, but the visualization might become overloaded

Using the energy distance to aggregate the information and visualizing it with radar charts, dendrograms, and heat maps have been found insightful when inspecting influencing factors such as different sites or different weather conditions.

Analysis of the in-season variable phenology

After analyzing the end-of-season variable yield, we now focus on time series of the in-season variables phenological development stage (BBCH) and leaf area index (LAI, "Analysis of the in-season variable leaf area index"). Exemplary plots of the BBCH time series for site 1, year 2011 are shown in Fig. 7. The corresponding plots for all site-years are provided in the Appendix (Fig. 25).

We start with a qualitative analysis of the time series in "Predictive distributions". Next, we quantify how similar or different the models behave at each daily time step by calculating the energy distance between the predictive distributions in "Energy distance-based similarity analysis". We compare this between-model distance to the spread within

Fig. 7 Time series of phenology predictions for site 1, year 2011. The shaded intervals represent the 90% credible intervals. The points represent the median of the replicate measurements

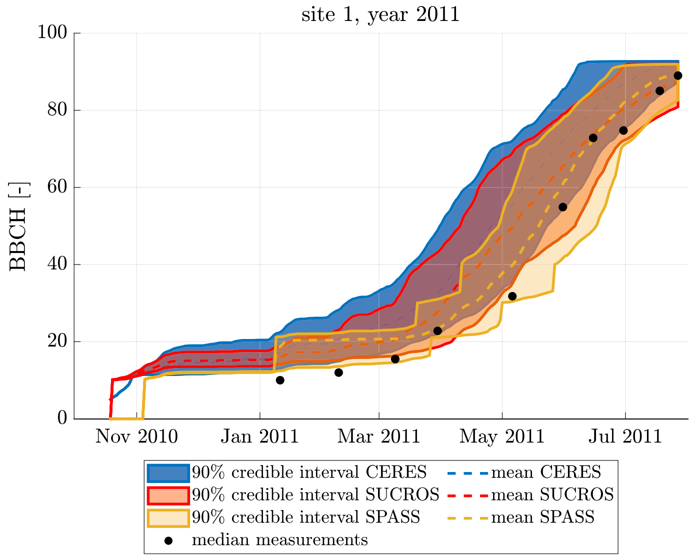

each model. This spread is calculated as the square root of the mean Euclidean distance between all samples of the predictive distribution (see Eq. 1).

In contrast to the analysis of the yield predictions, we do not assume a distribution for the measurement errors for BBCH or LAI. Therefore, we use the median of the replicates and calculate the energy score, i.e. the counterpart of the energy distance for comparing distributions to a single observation.

Predictive distributions

From Fig. 7 we can see that the prior predictive distributions for the development stage generated by SPASS show a very small variance until January, whereas the predictions of CERES and SUCROS initially have little variance, but the spread increases already in November. This can be observed for all site-years (see Fig. 25).

Comparing the predictions to the measurements shows that early BBCH stages are usually overestimated by all three models. Starting approximately in March, when the development stage reaches values of 20, the predictions become more accurate.

The mean predictions of SPASS are closest to the measurements for most site-years, while particularly CERES, and to a lesser extent SUCROS, overestimate earlier phenological development. The discernible steps in the SPASS simulations are a direct result of and consistent with the model structure: in contrast to the two other models, which represent the secondary growth stages as fractions of the temperature sums required for each principal growth stage (BBCH = 10–20, 20–30, 30–40, …), SPASS simulates the secondary growth stages during the early development (BBCH = 10–40) based on the number of emerged main stem leaves (BBCH = 11, 12, …), tillers (BBCH = 21, 22, …), and main stem nodes (BBCH = 31, 32, …) Wang and Engel (1998). Therefore, in this model simulated BBCH may not be a continuous function of time. For example, if only five main stem leaves have unfolded by the day on which the principal growth stage "tillering" (BBCH = 20) has been reached, a discontinuity from BBCH = 15 to BBCH = 20 would be simulated. The model behaves similarly with respect to the number of tillers on day of principal growth stage "stem elongation" (BBCH = 30) and the number of nodes at principal growth stage "booting" (BBCH = 40).

We note that the better predictions of BBCH by SPASS are in contrast to the worst performance in yield. We can put these results into perspective with the yield predictions. While our belief about plausible parameter ranges of SUCROS and CERES led to an early onset of BBCH development, on average, the grain filling period from anthesis (BBCH = 60) until maturity (BBCH = 90) is longest. The price of this is a worse match in BBCH, in contrast to SPASS. While SPASS reaches maturity approximately similarly as SUCROS, it is the shorter grain filling duration in SPASS that results in a tendency for lower yields, shown by the heavy tails on the left of the predictive distribution functions (see Figs. 2, 3).

For the stated reasons, this delayed BBCH development (i.e., not-achieved maturity, leading to lower grain yields) does not occur in CERES. From this insight, we can update our formulation of plausible parameter ranges by ensuring that the grain filling rate in the SPASS model parameters is increased. Similar updates are possible for SUCROS and CERES, where a delayed BBCH would have been matched with an increased grain filling rate. Since, in practice, fertilization dates are co-informed by BBCH, this result is of great significance to enhance the prior predictive capabilities of the models for these types of environments.

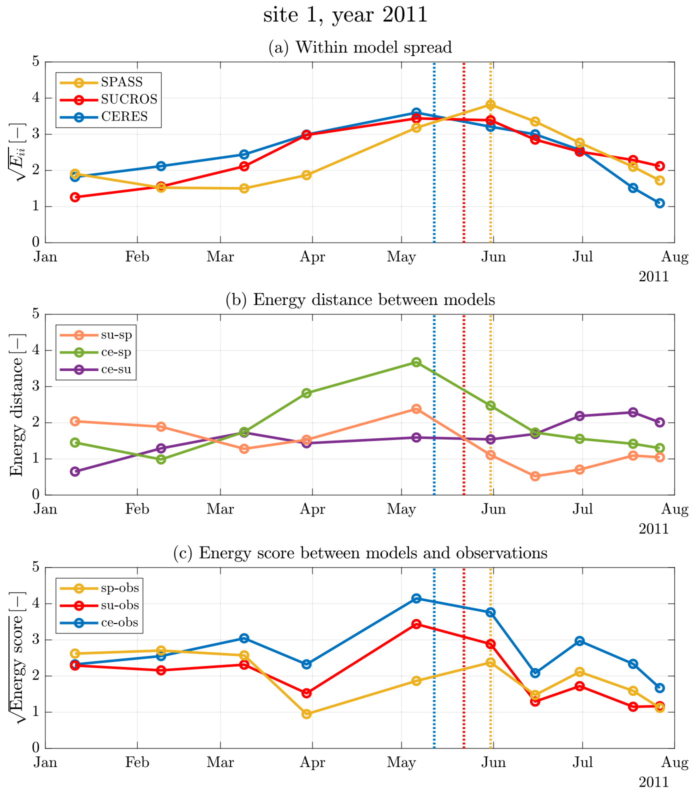

Fig. 8 **a** Within-model spread (square root of the mean Euclidean distance between the samples within each model) $\sqrt{E_{ii}}$, **b** energy distance d between pairs of models, and **c** root energy score $\sqrt{\text{ES}}$ between models and observations based on phenology predictions, site 1, year 2011. The dashed lines indicate the date when the mean predictions reach BBCH = 60

Energy distance-based similarity analysis

Figure 8 (a) shows time series of the spread of each model, (b) the energy distance between pairs of models and (c) the energy score between models and observations. The corresponding figures for all other site-years are provided in the Appendix (Figs. 19, 20, 21, 22, 23 and 24).

From Fig. 8 we can see phenomena that can be observed in most site-years: Within-model spreads of phenology predictions (Fig. 8a) show an increasing trend until June and decrease steadily thereafter. This is to be expected since all models aim at reaching fill plant maturity by the time of harvest. While the curves for CERES (blue) and SUCROS (red) are similar, the one representing SPASS (yellow) is often shifted towards a later maximum in July and therefore shows the highest spread in its predictions at harvest date. From this, we can identify that the largest predictive uncertainty occurs around BBCH = 60, although it is one of the most important predicted stages. Within all models, the anthesis date at BBCH=60 is very important, as it marks the point at which grain filling starts. In principle, a very late start and short grain filling period (visible as steep slopes in the curves after BBCH=60 in Fig. 7) can be compensated with implausibly high grain filling rate parameters, such that reasonable yields can nevertheless be simulated. This can be achieved in all of the models.

In Fig. 8b, we can analyze the distance, i.e. dissimilarity between pairs of models. The distance between CERES and SPASS (green curve) is the highest during most phases for all site-years. After reaching the maximum distance in May, it decreases again. The distance between SUCROS and SPASS (orange curve) shows a similar development, however, the distance between these models is smaller most of the time. The distance between CERES and SUCROS (purple curve) does not show this characteristic maximum in May, rather it increases more or less steadily over the season and thus, the difference between CERES and SUCROS becomes the highest at the harvest date.

The curves in Fig. 8c can be interpreted as the models' goodness-of-fit to measurements. A low energy score means a low distance to the observations and hence a good model performance. The time series of CERES and SUCROS show similar behavior with a maximum energy score in May to June, followed by a decline. For most site-years, CERES has the highest energy score. Although in some cases SPASS starts with the highest energy score, for most site-years, it is closest to the observations during most phases. Hence, from a model selection perspective, SPASS would be considered best overall. Nonetheless, the analysis with the energy score clearly shows that, especially in certain time windows, employing additional alternative models increases reliable predictive coverage.

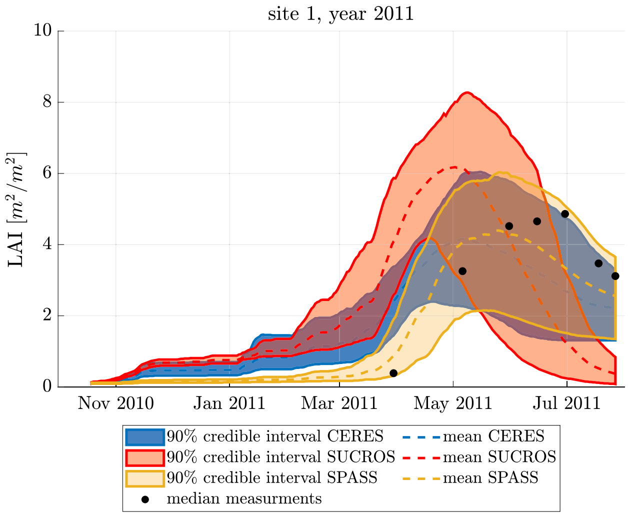

Fig. 9 Time series of LAI predictions for site 1, year 2011. The shaded intervals represent the 90% credible intervals

Analysis of the in-season variable leaf area index

Predictive distributions

After the analysis of BBCH, we now study the in-season variable LAI. Exemplary plots of the time series for site 1, year 2011 are shown in Fig. 9. The corresponding plots for all site-years are provided in the Appendix (Fig. 26).

The adopted measurement technique (Weber et al. 2021) for field observations of LAI does not differentiate between green leaf (i.e. photosynthetically active) and dead leaves. After the onset of leaf senescence, which dominates the LAI evolution after maximum LAI, we can consider that the measured LAI values contain an unknown amount of green leaf as well as dead leaves. However, the modeled LAI is green leaf LAI. For LAI, we can see clear differences between the predictions of the three models: CERES and SUCROS overestimate the LAI in the initial phase, however, the predictions of CERES do not drop as significantly as the ones of SUCROS. As for the phenological development, SPASS can describe the measured data most accurately.

In all cases, the peak of the median simulated LAI is much earlier than the peak in the measurements, sometimes by far. Since green leaf LAI of winter wheat is 0 at harvest, we see that, out of the three models, only a few individual simulation runs of SUCROS achieve this. Recall that the SUCROS wheat model does not simulate the vernalization of winter wheat. In other words, it is a summer wheat model, providing a feasible explanation of the, comparatively, very early development of LAI. This overestimation leads to a premature maximum and underestimates the measurements in the decreasing phase during senescence.

Figure 9 indicates that the prior predictive of SUCROS at harvest is close to zero, however with both an early and large peak in simulated LAI. Both CERES and SPASS are closer to the data but do not reach a green leaf of 0 at harvest. For SPASS this could relate to the fact that the simulated phenology had not fully reached maturity by the time of the harvest. In other words, if in the model the harvest date had been set to full maturity, and not to the farmer-reported harvest date, we would surely observe a further decrease in LAI. While the development stage of SPASS is “too slow”, we can learn that the senescence of CERES is not fast enough.

Energy distance-based similarity analysis

Similar to BBCH, the within-model spread of the LAI predictions in Fig. 10a increases slowly until June, followed by a decrease until harvest. The curves representing CERES and SPASS are relatively similar. SUCROS shows the largest spread for most of the simulation time until it declines starting in June. At the harvest date, it is mostly SPASS that has the highest spread in its predictions.

In Fig. 10b, the energy distance between the models shows that, during most of the seasons, the predictions of CERES and SPASS are the most similar ones. The time series of the energy distance between SUCROS and CERES and between SUCROS and SPASS are similar, with the ones of SUCROS and CERES being usually lower (i.e. the models are more similar) and showing a minimum in June–July, followed by a rising phase until harvest.

Figure 10c shows that SPASS has the lowest distance to the observations for most months, which means it performs best. The curve representing CERES’ energy score ranges in the middle, and SUCROS performs worst, having the highest distance. The case of SUCROS highlights one of the major benefits of analyzing model predictive distributions using energy distance and energy score: While SUCROS shows the worst predictions according to Fig. 10c, it provides these with the highest confidence in the time from July to August. Energy statistics support this insight in a straightforward way on an easily-interpretable scale.

Compared to the energy-statistics-based analysis of BBCH (Fig. 8), the within-model spreads of the LAI predictions (Fig. 10) are smaller and increase less during the growing season. From the energy distance between the models, we can observe that CERES and SPASS are the most dissimilar models with regard to BBCH predictions, while they are the most similar ones considering LAI predictions. Here, the biggest differences are between the LAI predictions of SUCROS and SPASS. The smallest energy score and, hence, the best goodness-of-fit during most phases was calculated, for both quantities of interest, by SPASS. The worst performing model regarding LAI predictions is SUCROS, while considering BBCH predictions, it is CERES.

Fig. 10 **a** Within-model spread (square root of the mean Euclidean distance between the samples within each model) $\sqrt{E_{ii}}$, **b** energy distance d between pairs of models, and **c** root energy score $\sqrt{\text{ES}}$ between models and observations based on LAI, site 1, year 2011

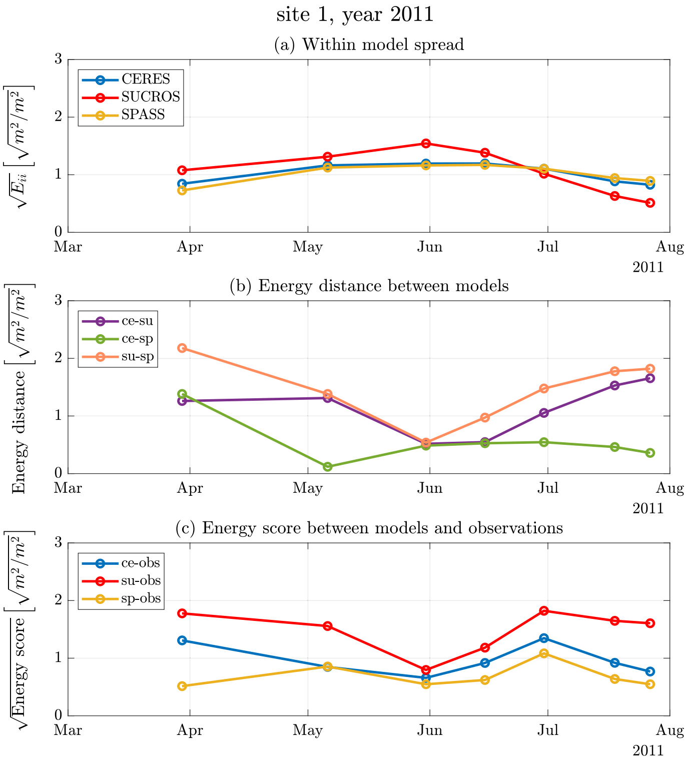

Our analysis of the prior predictive distributions revealed that a model that performs well during season might still end with an imprecise yield prediction: During the season, SPASS is best in predicting LAI and BBCH, whereas CERES and SUCROS clearly deviate from the observations, especially in the case of LAI. In predicting yield, however, SUCROS performs best, while SPASS is worst due to its very broad prior predictive distribution that covers even very low values with a relatively high probability. This confirms what was observed in the study by Martre et al. (2015). They compared the goodness-of-fit for calibrated models: a model that cannot reproduce in-season measurements well might do a better job in predicting end-of-season variables. Given our analysis, one could add to this statement that also the reverse can be true, i.e. a model that performs well during the season might still fail to predict yield reasonably.

In addition, the similarity among the models was not consistent across different variables: while the LAI predictions of CERES and SPASS are the most similar ones and the ones of SUCROS and SPASS are the most dissimilar ones, the opposite is true considering the yield predictions.

Summary and conclusions

We analyzed the similarity of predictions by the three plant growth models CERES, SPASS and SUCROS and their goodness-of-fit to observed data in a probabilistic framework. The goal of this study was to find methods for gaining deeper insights into the model set. An intuitive understanding of similarities between the models and the measurements can help model developers to improve both the individual models and the multi-model methods. The presented method can be used to identify different model settings, e.g. situations in which all models form a cluster while being distant from the measured data. This may indicate that all models are highly similar and that a relevant process is not considered in any of the models. An intuitive visualization of model similarities can guide the multi-model process, e.g. when it comes to assigning model weights for averaging. Therefore, we propose to combine specific visualization methods that make modelers aware of the (dis)similarities in the predictions of the considered model set. Each method highlights another piece of information and adds to a comprehensive overview of the considered model set.

The analysis is based on so-called energy statistics introduced by Rizzo and Székely (2016). The energy distance between the probabilistic predictions is used to quantify model similarities. With the same method, we can also assess model performance by calculating the energy distance between model predictions and noisy measurements. For comparing probabilistic model predictions to deterministic observations, the so-called energy score is used. It acts on the same scale as the energy distance making both intuitively comparable. Therefore, energy statistics proved to be widely applicable, as energy distance and energy score can be used jointly to compare two probability distributions as well as a probability distribution and a deterministic reference.

Our results confirmed that "there is no single best model" (Hagedorn et al. 2005; Palosuo et al. 2011; Martre et al. 2015): none of the investigated models performed consistently better or worse than the others when considering different variables. While SPASS showed the best goodness-of-fit regarding in-season variables LAI and BBCH, its overly wide yield predictions lead to poor performance for this end-of-season variable. Therefore, combining the models in an ensemble might indeed give more robust predictions as a broader range of possible predictions is covered.

Generally, we suggest analyzing model similarities when using multi-model ensembles, as redundancies in the model set lead to an overly high weight of certain predictions and therefore, model weights should be diluted (George 2010; Garthwaite and Mubwandarikwa 2010). Similar to the results regarding goodness-of-fit, we also found that model similarities vary for different variables: two models that gave similar predictions for one variable showed clear differences in predicting another one. Therefore, no general dilution priors can be defined for this model set. Rather, they need to be chosen depending on model similarities for each quantity of interest.

We also investigated whether model similarities or performance are dependent on the weather conditions during the growing season. To this end, we used radar charts to visualize the similarities and color-coded them according to the wetness or dryness of the respective site-year. Although there was no apparent effect of the weather conditions on the model predictions visible, we suggest this approach of visualization to be studied further. We assume that, for other scenarios and model sets, this might be a straightforward tool to display the influence of different boundary conditions on the prediction accuracy and similarity of models. By assessing the within-model spread, the distance between the models, and the goodness-of-fit on the same scale, we can gain a better understanding of the model set.

Our study was based on prior predictions, i.e. the models have not been calibrated. There are two main reasons for this: (1) (not only) in the crop modeling community, different groups use different calibration approaches (Wallach et al. 2020) and hence, there is a lack of consistency. (2) Model structural errors are often compensated by choosing non-physical parameters (e.g. Wallach 2011). This leads to good model performance for the variable the model has been calibrated on, but poor performance for others. Therefore, we support the suggestion of Vogel and Sankarasubramanian (2003) to validate the model structure prior to calibration. As in any Bayesian framework, a subjective choice of prior distributions based on expert knowledge is needed. Future research should assess the sensitivity of the analysis regarding the priors. Another promising way to go is the assessment of structural model similarity, e.g. based on information-theoretic methods as done by Bennett et al. (2019). As our analysis suggests that a combination of the individual models into an ensemble prediction might yield more robust results, our introduced model evaluation workflow might also inform different model combination methods and weighting schemes of future applications.

Appendix 1: Model description

See Tables 3, 4, 6, 5, 7.

Table 3 Characteristics of the three models, adapted from Asseng et al. (2013), supplementary material (Table S2)

	CERES	SPASS	SUCROS
Leaf area/light interception	Simple	Detailed	Detailed
Light utilization	Radiation use efficiency approach	Gross photosynthesis-respiration	Gross photosynthesis-respiration
Yield formation	Tot. (above-ground) biomass, number of grains	Number of grains, partitioning during reproductive stages	Partitioning during reproductive stages
Phenology	Temperature, photoperiod (day length), vernalization	Temperature, photoperiod (day length), vernalization	Temperature
Root distribution over depth	Exponential	Exponential	Exponential
Environmental constraints	Water limitation, *N* limitation	Water limitation, *N* limitation	Water limitation, *N* limitation
Type of water stress	Actual to potential evapotranspiration ratio, soil available water in root zone	Actual to potential evapotranspiration ratio, soil available water in root zone	Actual to potential evapotranspiration ratio, soil available water in root zone
Water dynamics	Richards approach	Richards approach	Richards approach
Evapotranspiration	Penman–Monteith	Penman–Monteith	Penman–Monteith
Soil CN-model	CN model, 3 organic matter pools, microbial biomass pool	CN model, 3 organic matter pools, microbial biomass pool	CN model, 3 organic matter pools, microbial biomass pool
No. of cultivar parameters	7	5	2

Table 4 Description of model parameters varied and parameter bounds of the uniform prior where a = lower bound and b = upper bound, subscript 1 denotes the top-soil and 2 the sub-soil as defined in Table 1

Module	Parameter	Unit	a	b	Description
Soil water	α_1, α_2	cm^{-1}	0.002	0.03	van Genuchten α
	n_1, n_2	–	1.2	2.2	van Genuchten n
	$K_{s,1}, K_{s,2}$	cm d^{-1}	10	500	saturated hydraulic conductivity
	τ_1, τ_1	–	− 1	8	Tortuousity parameter
ET_a	kc_{ini}	–	0.2	1	Crop coefficient for the initial vegetation period (dev stage 0)
	kc_{mid}	–	0.5	1.8	Crop coefficient for the mid vegetation period (dev stage 0.75–1.5)
	kc_{end}	–	0.2	1	Crop coefficient for the end of the vegetation period (dev stage 2.0)
Nitrogen	Nit_1	d^{-1}	0.1	1	Nitrification rate
	Nit_2	d^{-1}	0.05	0.6	
	DeNit_1	d^{-1}	0.1	1	Denitrification rate
	DeNit_2	d^{-1}	0.0	0.01	
	MiLit_1	d^{-1}	0.01	0.1	Mineralization rate constant of the litter pool
	MiLit_2	d^{-1}	0.01	0.1	
	MiHum_1	d^{-1}	$1e^{-5}$	$1e^{-4}$	Mineralization rate constant of the humus pool
	MiHum_2	d^{-1}	$1e^{-6}$	$1e^{-5}$	
	MiMa	d^{-1}	0.01	0.1	Mineralization rate constant of the manure pool
Initial condition	$\theta_{ini,1}$	vol%	10	40	Initial soil profile water content
	$\theta_{ini,2}$	vol%	15	45	

Table 5 Description of SPASS model parameters and parameter bounds of the prior

Parameter	Unit	*a*	*b*	Description
PMAX	$\mathrm{kg}_{\mathrm{CO}_2}\ \mathrm{ha}_{\mathrm{leaf}}^{-1}\ h^{-1}$	38	45	Gross photosynthesis rate at light saturation and CO_2 340 ppm
LUE	$\mathrm{g\ J}^{-1}$	0.55	0.7	Light use efficiency
TMINPS	°C	0	5	Minimum temperature for photosynthesis
TOPTPS	°C	20	25	Optimum temperature for photosynthesis
TMAXPS	°C	32	40	Maximum temperature for photosynthesis
PDD1	d	32	48	Duration from emergence to anthesis
PDD2	d	20	36	Duration from anthesis to emergence
VERN	d	24	46	Minimum value of vernalization days
PDL	–	0.01	0.25	Photoperiod sensitivity factor
DLOPT	h	18	20	Optimal photoperiod length
TMINDEV	°C	0	2	Minimum temperature of vegetative development
TOPTDEV	°C	22	26	Optimum temperature of vegetative development
TMAXDEV	°C	32	38	Maximum temperature of vegetative development
TMINDEV2	°C	2	6	Minimum temperature of reprod. development
TOPTDEV2	°C	26	30	Optimum temperature of reprod. development
TMAXDEV2	°C	38	45	Maximum temperature of reprod. development
G1	$\#\mathrm{g}^{-1}$	24	35	Number of grains per stem weight at anthesis
SPCLW	$\mathrm{kg}_{\mathrm{DW}}\ \mathrm{ha}_{\mathrm{leaf}}^{-1}$	350	500	Specific leaf weight
RESR	–	0.36	0.45	Fraction of stem weight as reserves
G2	$\mathrm{mg\ grain}^{-1}\ \mathrm{d}^{-1}$	2.4	3.6	Maximum grain filling rate
NACCR	$\mathrm{mg}_{\mathrm{N}}\ \mathrm{grain}^{-1}\ \mathrm{d}^{-1}$	0.02	0.06	Nitrogen accumulation rate
REXT	$\mathrm{cm\ d}^{-1}$	1.5	3.0	Maximum root extension rate
SPCRL	$\mathrm{cm\ g}^{-1}$	8000	12000	Specific root length
RWUR	$\mathrm{cm}^3\ \mathrm{cm}^{-1}\ \mathrm{d}^{-1}$	0.024	0.036	Maximum water uptake rate per root length
RNUR	$\mathrm{kg}_{\mathrm{N}}\ \mathrm{cm}^{-1}\ \mathrm{d}^{-1}$	0.006	0.01	Maximum nitrogen uptake rate per root length
RDMAX	cm	100	200	Maximum rooting depth
DVSSEN	–	1	1.3	Development stage at which senescence begins
RDRL	–	0.015	0.025	Relative death rate of leaves
RDRR	–	0.015	0.025	Relative death rate of roots

Table 6 Description of CERES model parameters and parameter bounds of the prior

Parameter	Unit	*a*	*b*	Description
P1D	–	0.001	0.008	Daylength coefficient
P1V	h	25	60	Inverse of optimum vernalization rate
PHINT	–	70	150	Phyllochrone interval
P1	°C d	170	400	Thermal Time from emergence-to terminal spikelet
P4	°C d	120	200	Thermal Time from end of pre-anthesis ear growth-begin of grain filling
P5	°C d	400	700	Thermal Time for grain filling (phase 5)
G1	$\#\mathrm{g}^{-1}$	20	40	Number of grains per stem weight at anthesis
G2	$\mathrm{mggrain}^{-1}\ \mathrm{d}^{-1}$	1	4	Maximum grain filling rate
RWUR	$\mathrm{cm}^3\ \mathrm{cm}^{-1}\ \mathrm{d}^{-1}$	0.01	0.1	Maximum water uptake rate per root length
RNUR	$\mathrm{kg\ ha}^{-1}$	0.003	0.027	Maximum nitrogen uptake rate per root length

Table 7 Description of SUCROS model parameters and parameter bounds of the prior

Parameter	Unit	*a*	*b*	Description
PMAX	$\mathrm{kg}_{\mathrm{CO_2}}\ \mathrm{ha}_{\mathrm{leaf}}^{-1}\ h^{-1}$	38	45	Gross photosynthesis rate at light saturation and CO_2 340 ppm
LUE	g J^{-1}	0.55	0.7	Light use efficiency
TBASE1	°C	0	2	Base temperature for phen. dev. vegetative phase
TSUM1	°C d	700	1500	Temperature sum of vegetative growth phase
TBASE2	°C	2	5	Base temperature for phen. dev. generative phase
TSUM2	°C d	600	1400	Temperature sum of generative growth phase
LA0	$\mathrm{m}^2\ \mathrm{plant}^{-1} * 10{,}000$	0.45	0.7	Initial leaf area
RGRL	$°\mathrm{C}^{-1}\ \mathrm{d}^{-1}$	0.005	0.01	Relative growth rate of leaf area
G1	$\#\mathrm{g}^{-1}$	24	35	Number of grains per stem weight at anthesis
SPCLW	$\mathrm{kg}_{\mathrm{DW}}\ \mathrm{ha}_{\mathrm{leaf}}^{-1}$	350	500	Specific leaf weight
REXT	cm d^{-1}	1.5	3.0	Maximum root extension rate
SPCRL	m kg^{-1}	8000	12,000	Specific root length
RDMAX	cm	100	200	Maximum rooting depth

Appendix B: Figures

See Figs. 11, 12, 13, 14, 15, 16, 17, 18, 19, 20, 21, 22, 23, 24, 25 and 26.

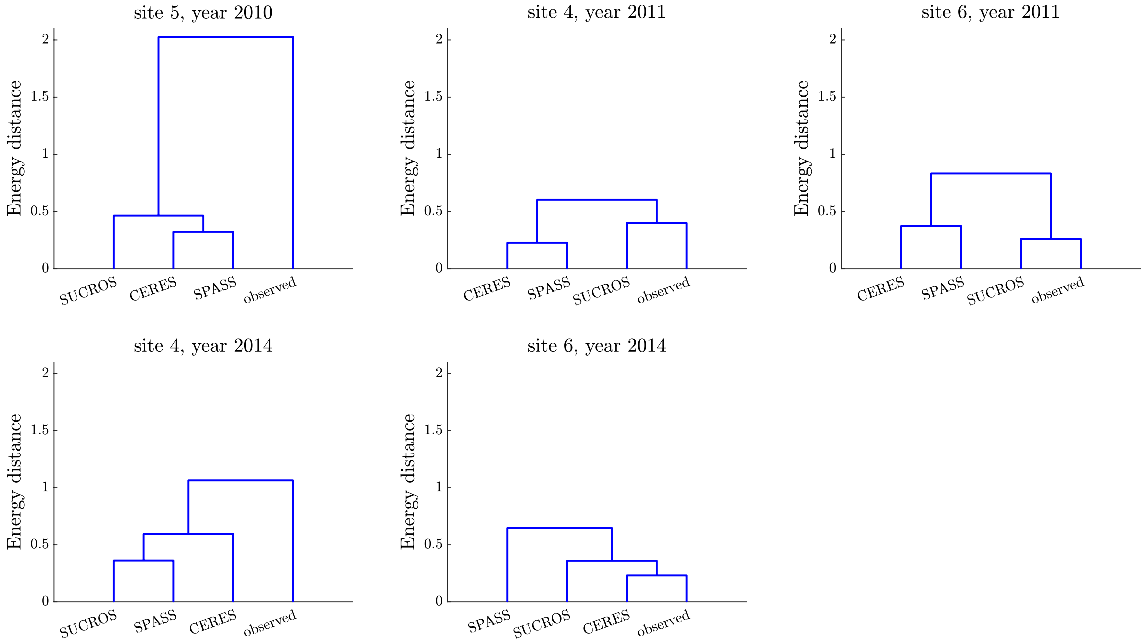

Fig. 11 Dendrograms based on the energy distance between models and observations (yield predictions)

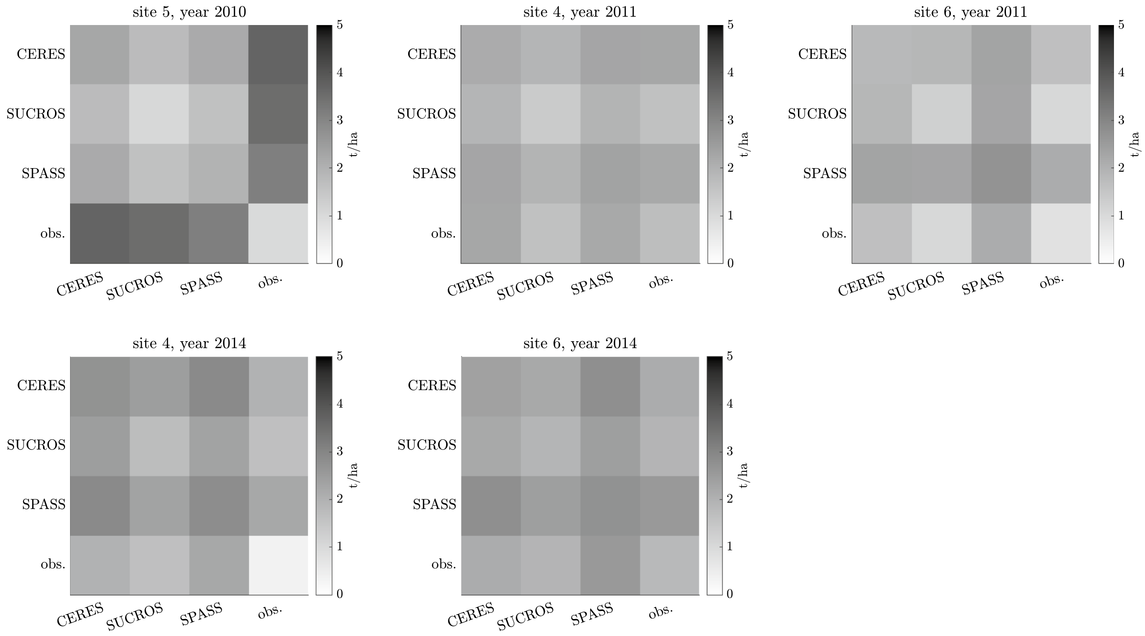

Fig. 12 Heatmap reflecting the similarities between models and observations based on yield predictions for site 4–6. The color-coding represents the values of the individual components of the energy distance: $\mathbb{E}||X - Y||_2$ (main diagonal entries) and $\mathbb{E}||X - X'||_2$ (off-diagonal entries)

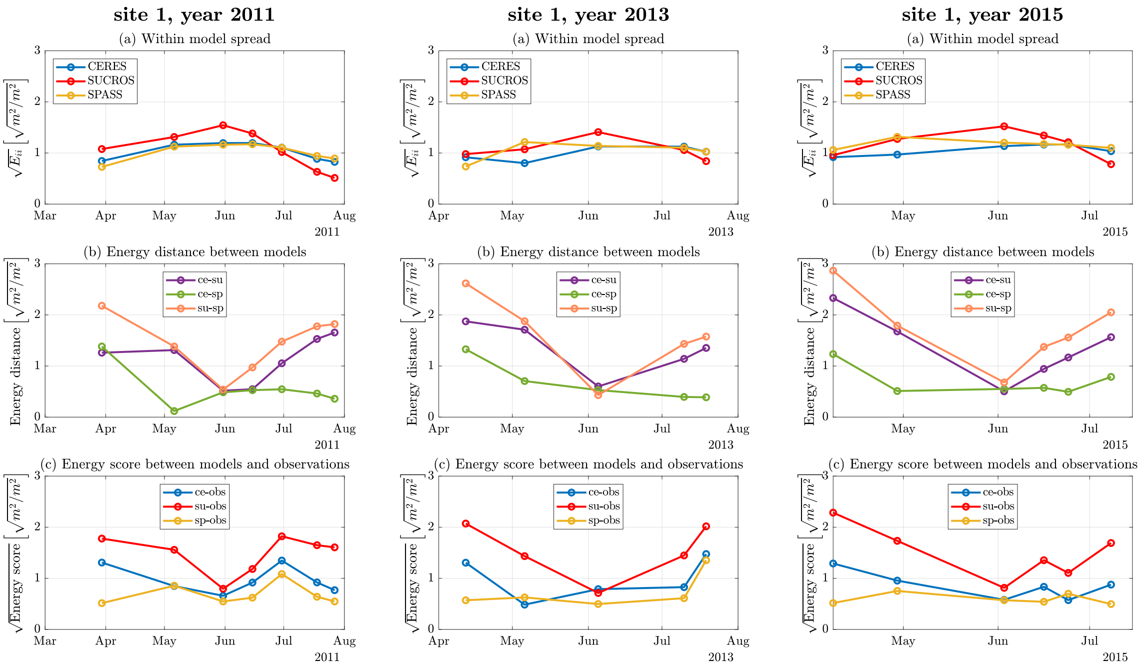

Fig. 13 **a** Within-model spread (square root of the mean Euclidean distance between the samples within each model) $\sqrt{E_{ii}}$, **b** energy distance d between pairs of models, and **c** root energy score $\sqrt{\text{ES}}$ between models and observations based on LAI for site 1

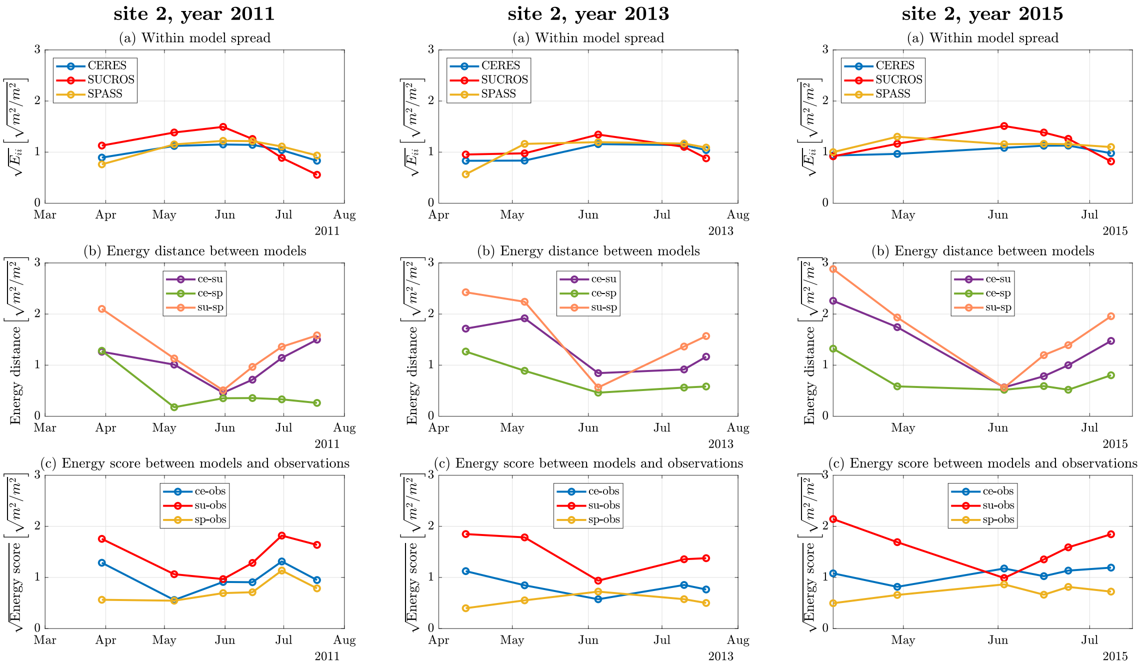

Fig. 14 **a** Within-model spread (square root of the mean Euclidean distance between the samples within each model) $\sqrt{E_{ii}}$, **b** energy distance d between pairs of models, and **c** root energy score $\sqrt{\text{ES}}$ between models and observations based on LAI for site 2

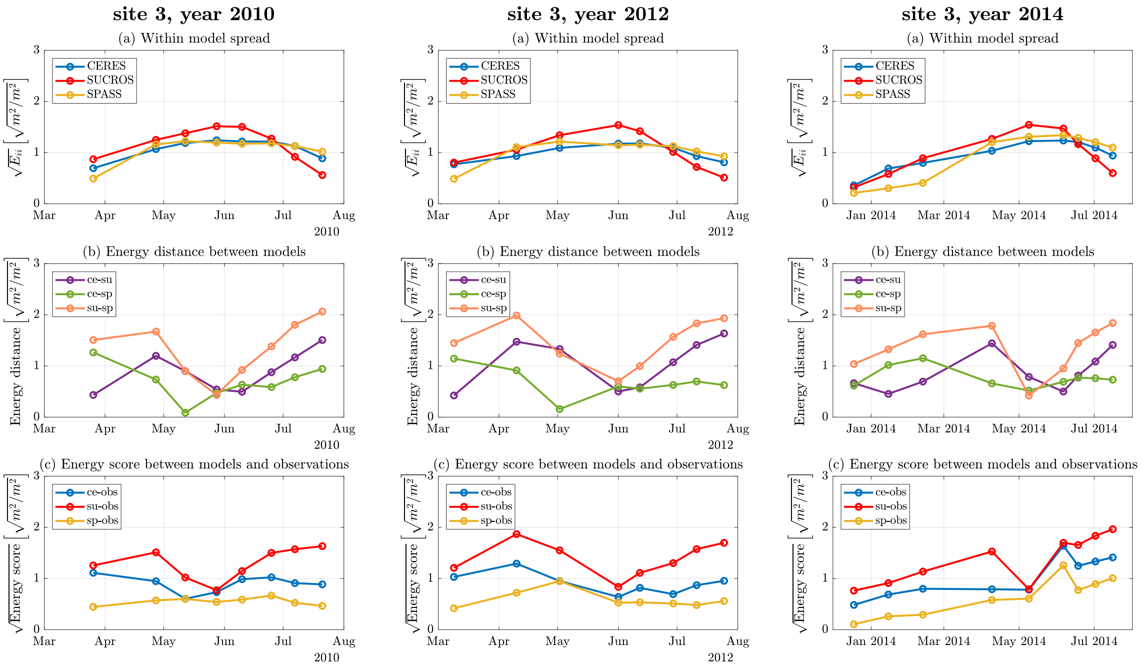

Fig. 15 **a** Within-model spread (square root of the mean Euclidean distance between the samples within each model) $\sqrt{E_{ii}}$, **b** energy distance d between pairs of models, and **c** root energy score $\sqrt{\text{ES}}$ between models and observations based on LAI for site 3

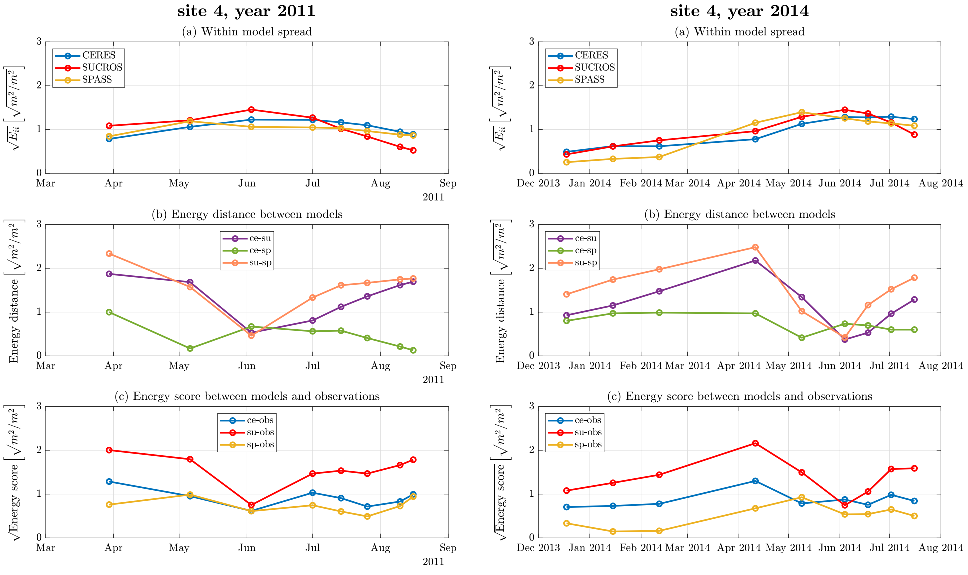

Fig. 16 **a** Within-model spread (square root of the mean Euclidean distance between the samples within each model) $\sqrt{E_{ii}}$, **b** energy distance d between pairs of models, and **c** root energy score $\sqrt{ES}$ between models and observations based on LAI for site 4

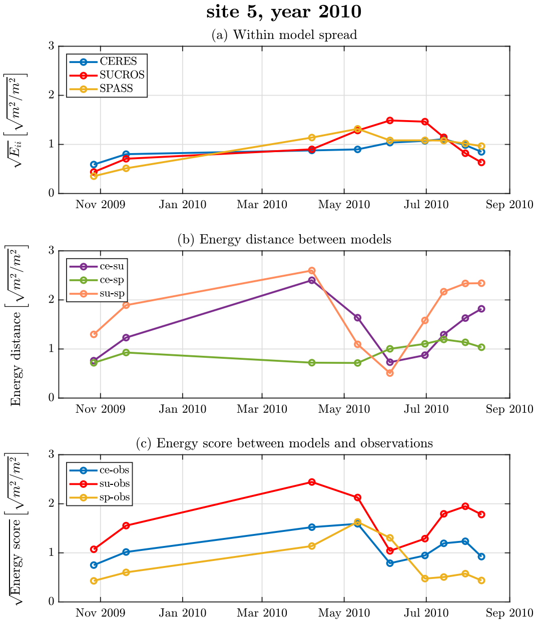

Fig. 17 **a** Within-model spread (square root of the mean Euclidean distance between the samples within each model) $\sqrt{E_{ii}}$, **b** energy distance d between pairs of models, and **c** root energy score $\sqrt{ES}$ between models and observations based on LAI for site 5

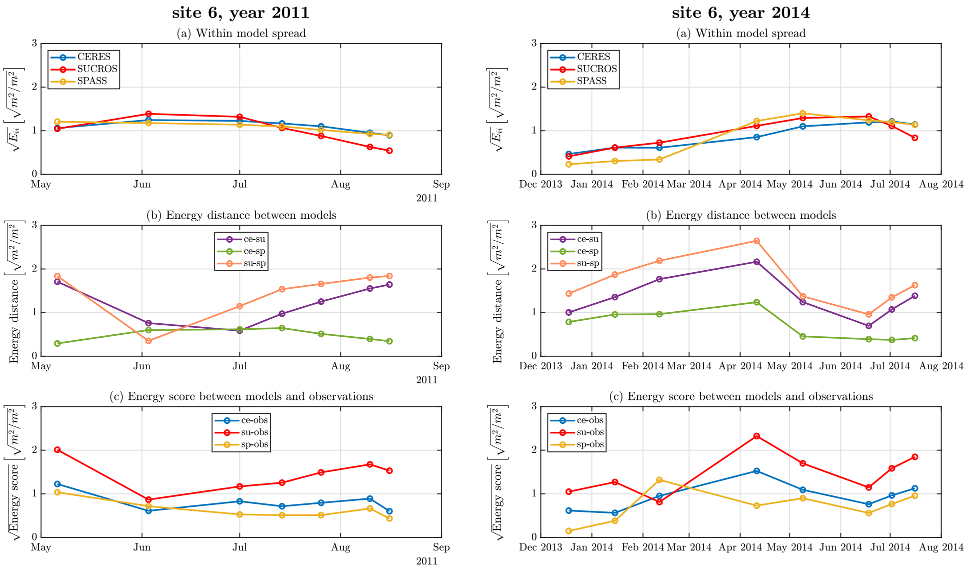

Fig. 18 **a** Within-model spread (square root of the mean Euclidean distance between the samples within each model) $\sqrt{E_{ii}}$, **b** energy distance d between pairs of models, and **c** root energy score $\sqrt{\text{ES}}$ between models and observations based on LAI for site 6

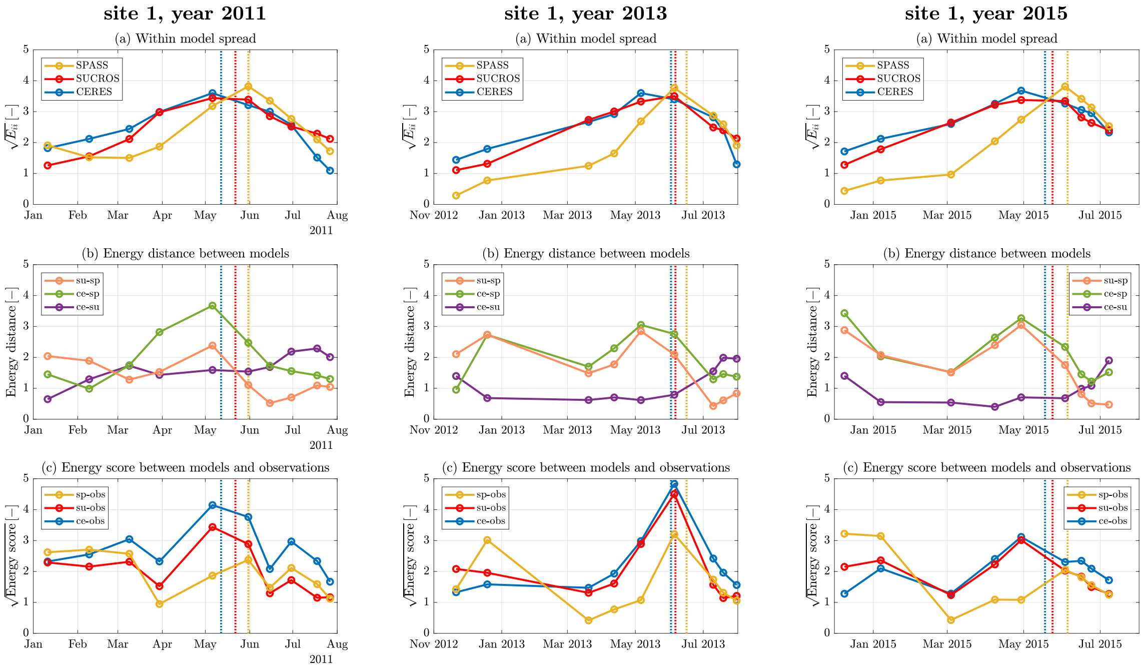

Fig. 19 **a** Within-model spread (square root of the mean Euclidean distance between the samples within each model) $\sqrt{E_{ii}}$, **b** energy distance d between pairs of models, and **c** root energy score $\sqrt{\text{ES}}$ between models and observations based on phenology for site 1. The dashed lines indicate the date when the mean predictions reach BBCH = 60

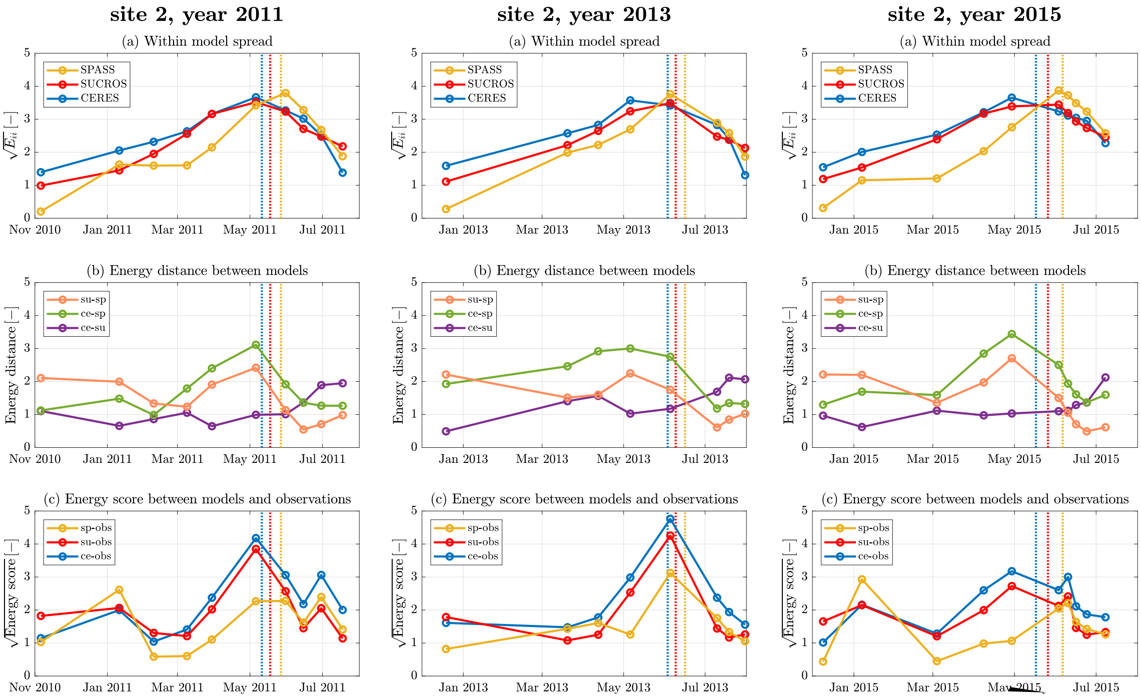

Fig. 20 **a** Within-model spread (square root of the mean Euclidean distance between the samples within each model) $\sqrt{E_{ii}}$, **b** energy distance d between pairs of models, and **c** root energy score $\sqrt{\text{ES}}$ between models and observations based on phenology for site 2. The dashed lines indicate the date when the mean predictions reach BBCH = 60

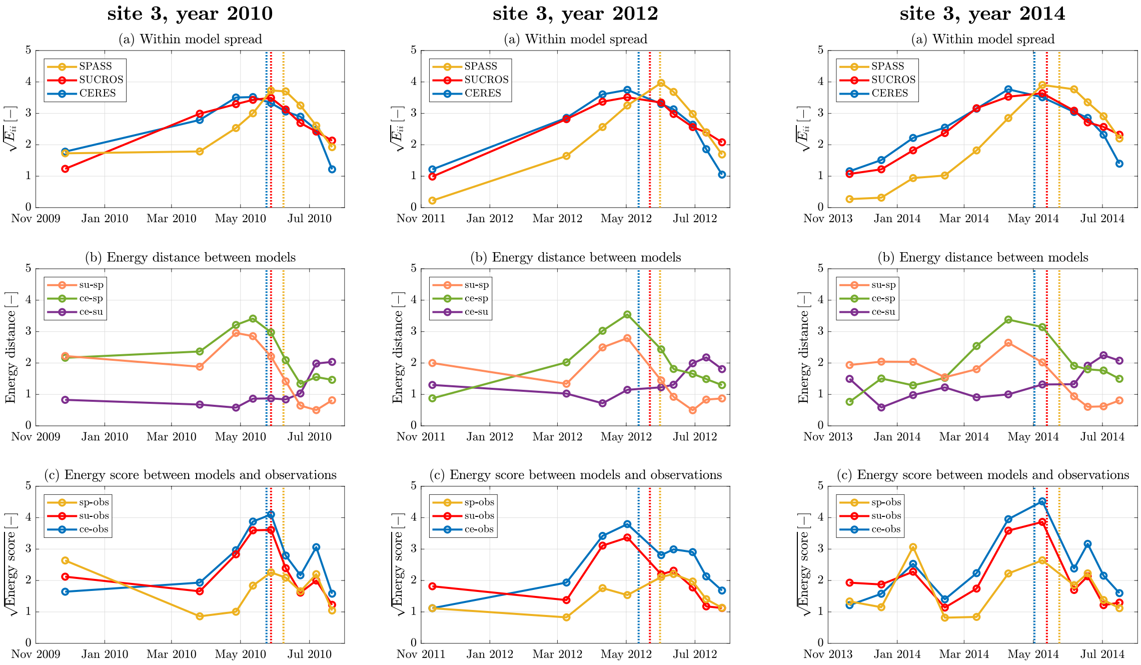

Fig. 21 **a** Within-model spread (square root of the mean Euclidean distance between the samples within each model) $\sqrt{E_{ii}}$, **b** energy distance d between pairs of models, and **c** root energy score $\sqrt{\text{ES}}$ between models and observations based on phenology for site 3. The dashed lines indicate the date when the mean predictions reach BBCH = 60

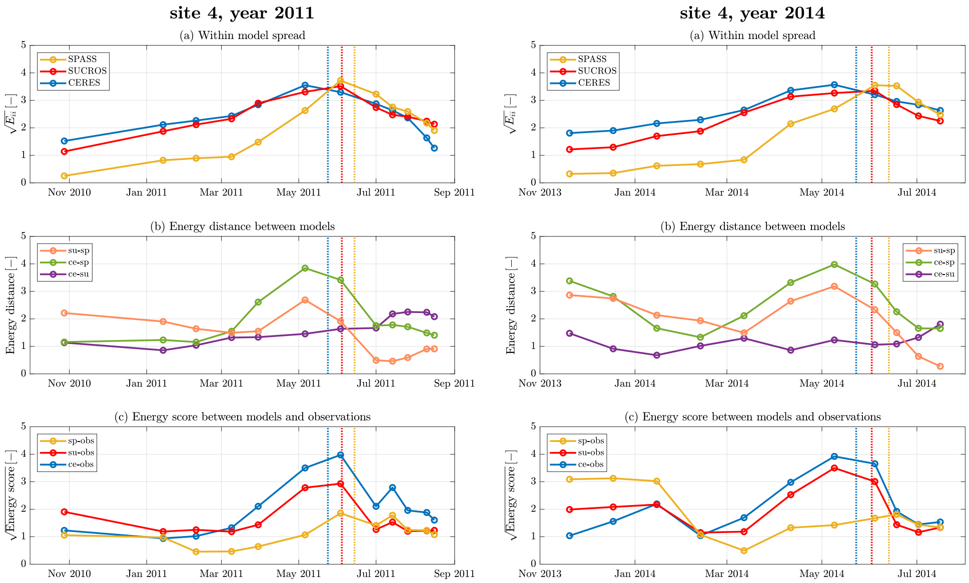

Fig. 22 **a** Within-model spread (square root of the mean Euclidean distance between the samples within each model) $\sqrt{E_{ii}}$, **b** energy distance d between pairs of models, and **c** root energy score $\sqrt{\text{ES}}$ between models and observations based on phenology for site 4. The dashed lines indicate the date when the mean predictions reach BBCH = 60

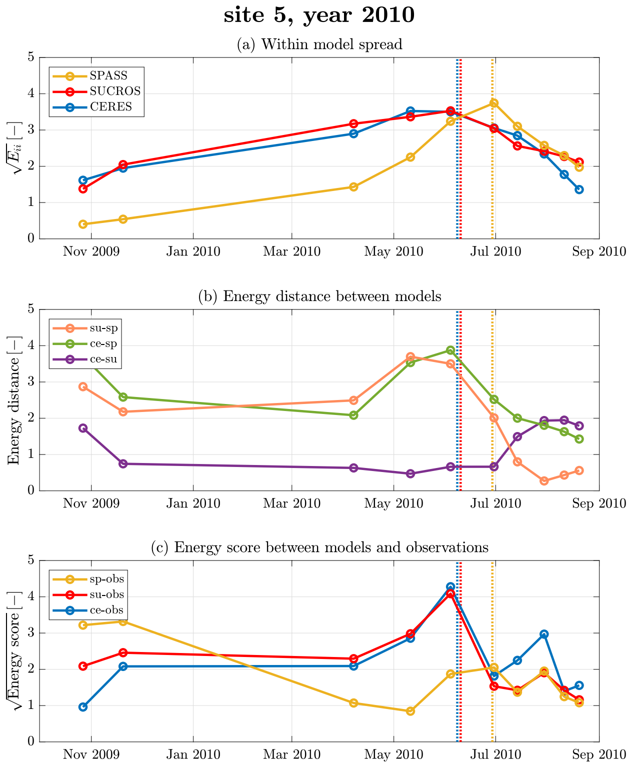

Fig. 23 **a** Within-model spread (square root of the mean Euclidean distance between the samples within each model) $\sqrt{E_{ii}}$, **b** energy distance d between pairs of models, and **c** root energy score $\sqrt{\text{ES}}$ between models and observations based on phenology for site 5. The dashed lines indicate the date when the mean predictions reach BBCH = 60

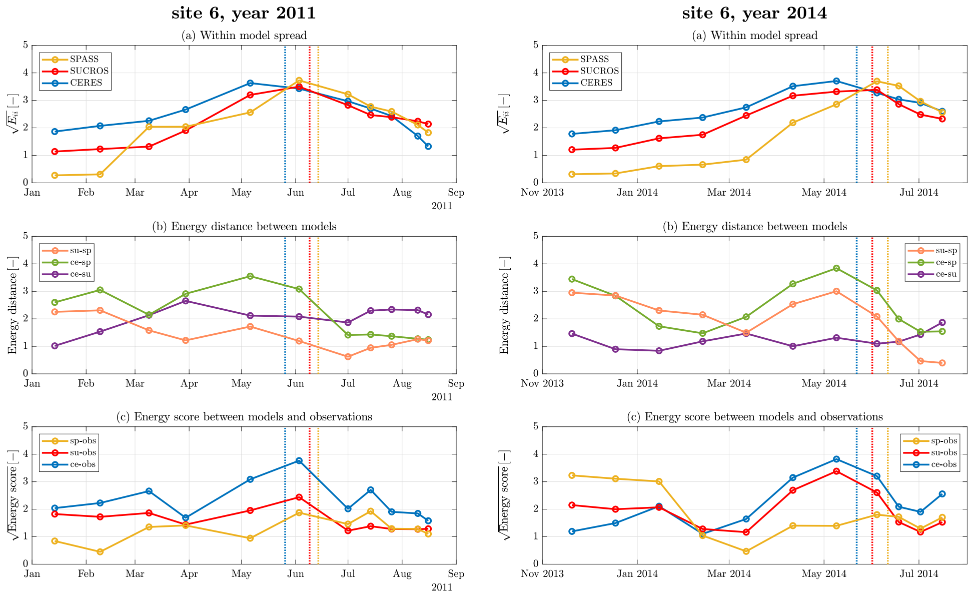

Fig. 24 **a** Within-model spread (square root of the mean Euclidean distance between the samples within each model) $\sqrt{E_{ii}}$, **b** energy distance d between pairs of models, and **c** root energy score $\sqrt{\text{ES}}$ between models and observations based on phenology for site 6. The dashed lines indicate the date when the mean predictions reach BBCH = 60

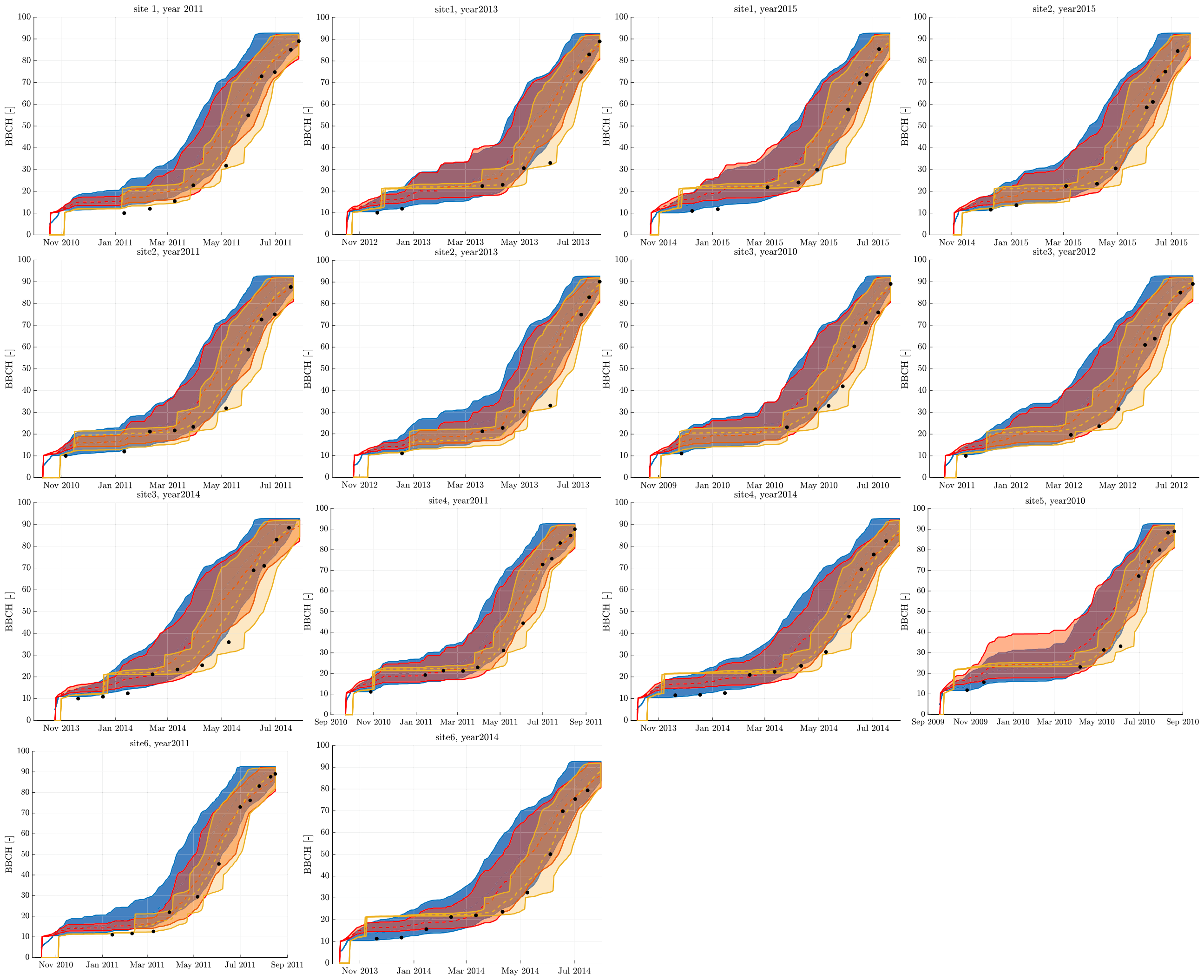

Fig. 25 Time series of phenology predictions for all site-years. The shaded intervals represent the 90% credible intervals (blue: CERES, red: SUCROS, yellow: SPASS), the dashed lines represent the model means and the black points represent the medians of the measurements

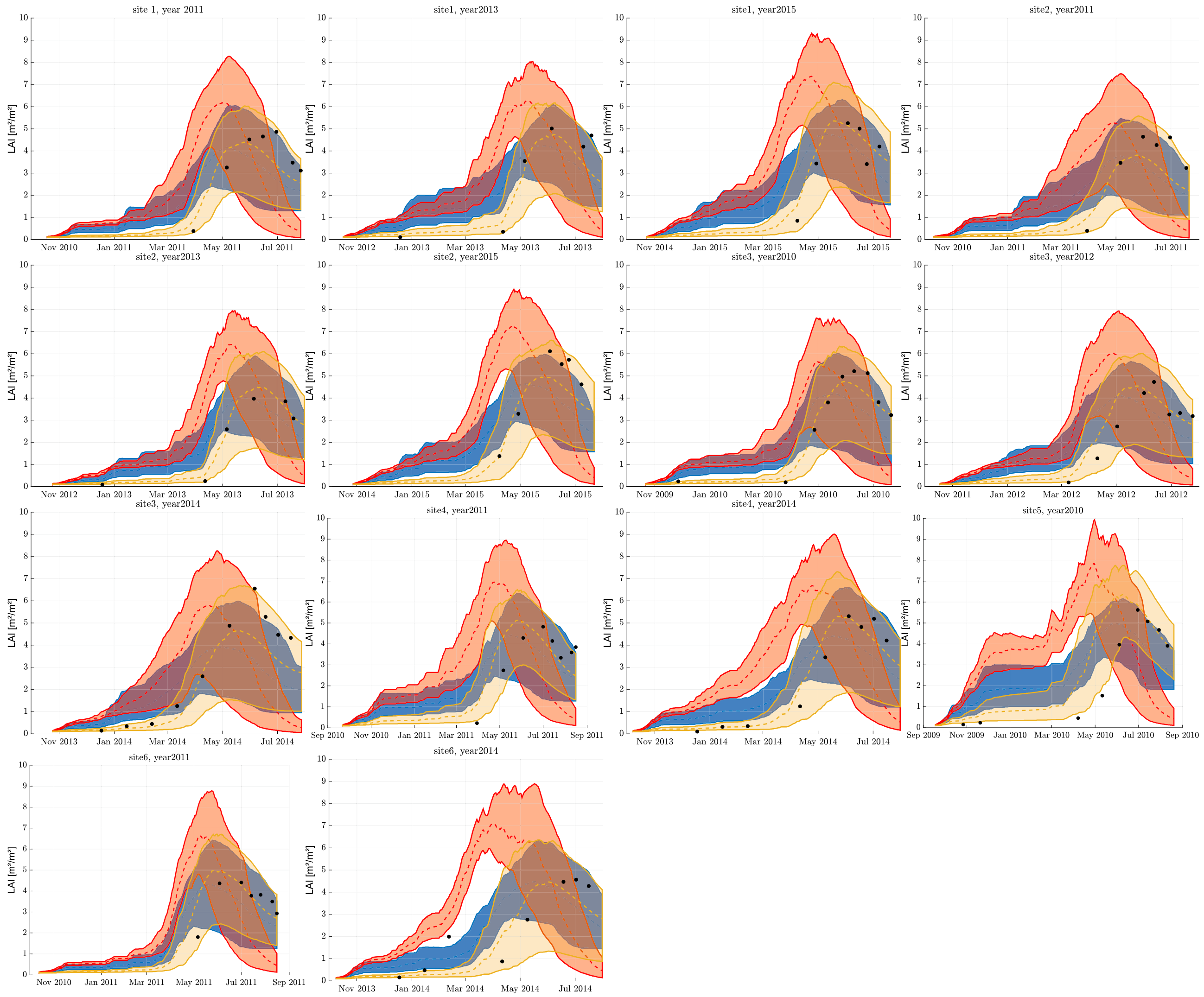

Fig. 26 Time series of LAI predictions for all site-years. The shaded intervals represent the 90% credible intervals (blue: CERES, red: SUCROS, yellow: SPASS), the dashed lines represent the model means and the black points represent the medians of the measurements

Acknowledgements The authors would like to thank the German Research Foundation (DFG) for financial support of the project within the Collaborative Research Center 1253 CAMPOS (DFG, Grant Agreement SFB 1253/1 2017) and the Cluster of Excellence EXC 2075 "Data-integrated Simulation Science (SimTech)" at the University of Stuttgart under Germany's Excellence Strategy-EXC 2075-390740016. We also thank Dr. Irene Witte for providing the Monte Carlo simulation results.

Funding Open Access funding enabled and organized by Projekt DEAL.

Data availibility Data and code can be downloaded here: https://bwsyncandshare.kit.edu/s/4gZZf4qEAA4TFMn.

References

Abramowitz G (2010) Model independence in multi-model ensemble prediction. Aust Meteorol Oceanogr J 59(1SP):3–6. https://doi.org/10.22499/2.5901.002

Abramowitz G, Gupta H (2008) Toward a model space and model independence metric. Geophys Res Lett. https://doi.org/10.1029/2007GL032834

Abramowitz G, Herger N, Gutmann E, Hammerling D, Knutti R, Leduc M, Lorenz R, Pincus R, Schmidt GA (2018) Model dependence in multi-model climate ensembles: weighting, sub-selection and out-of-sample testing. Earth Syst Dyn Discuss. https://doi.org/10.5194/esd-2018-51

Allen RG (1998) Crop evapotranspiration: guidelines for computing crop water requirements. FAO irrigation and drainage paper, vol. 56. FAO, Rome

Arsenault R, Gatien P, Renaud B, Brissette F, Martel J-L (2015) A comparative analysis of 9 multi-model averaging approaches in hydrological continuous streamflow simulation. J Hydrol 529:754–767. https://doi.org/10.1016/j.jhydrol.2015.09.001

Asseng S, Ewert F, Rosenzweig C, Jones JW, Hatfield JL, Ruane AC, Boote KJ, Thorburn PJ, Rötter RP, Cammarano D, Brisson N, Basso B, Martre P, Aggarwal PK, Angulo C, Bertuzzi P, Biernath C, Challinor AJ, Doltra J, Gayler S, Goldberg R, Grant R, Heng L, Hooker J, Hunt LA, Ingwersen J, Izaurralde RC, Kersebaum KC, Müller C, Naresh Kumar S, Nendel C, O'Leary G, Olesen JE, Osborne TM, Palosuo T, Priesack E, Ripoche D, Semenov MA, Shcherbak I, Steduto P, Stöckle C, Stratonovitch P, Streck T, Supit I, Tao F, Travasso M, Waha K, Wallach D, White JW, Williams JR, Wolf J (2013) Uncertainty in simulating wheat yields under climate change. Nat Clim Change 3(9):827–832. https://doi.org/10.1038/nclimate1916

Asseng S, Ewert F, Martre P, Rötter RP, Lobell DB, Cammarano D, Kimball BA, Ottman MJ, Wall GW, White JW, Reynolds MP, Alderman PD, Prasad PVV, Aggarwal PK, Anothai J, Basso B, Biernath C, Challinor AJ, deSanctis G, Doltra J, Fereres E, GarciaVila M, Gayler S, Hoogenboom G, Hunt LA, Izaurralde RC, Jabloun M, Jones CD, Kersebaum KC, Koehler A-K, Müller C, NareshKumar S, Nendel C, O'Leary G, Olesen JE, Palosuo T, Priesack E, EyshiRezaei E, Ruane AC, Semenov MA, Shcherbak I, Stöckle C, Stratonovitch P, Streck T, Supit I, Tao F, Thorburn PJ, Waha K, Wang E, Wallach D, Wolf J, Zhao Z, Zhu Y (2015) Rising temperatures reduce global wheat production. Nat Clim Change 5(2):143–147. https://doi.org/10.1038/NCLIMATE2470

Bennett A, Nijssen B, Ou G, Clark M, Nearing G (2019) Quantifying Process connectivity with transfer entropy in hydrologic models. Water Resour Res. https://doi.org/10.1029/2018WR024555

Biernath C, Gayler S, Bittner S, Klein C, Högy P, Fangmeier A, Priesack E (2011) Evaluating the ability of four crop models to predict different environmental impacts on spring wheat grown in open-top chambers. Eur J Agron 35(2):71–82. https://doi.org/10.1016/j.eja.2011.04.001

Bishop CH, Abramowitz G (2013) Climate model dependence and the replicate Earth paradigm. Clim Dyn 41(3–4):885–900. https://doi.org/10.1007/s00382-012-1610-y

Christiansen B (2018) Ensemble averaging and the curse of dimensionality. J Clim 31(4):1587–1596. https://doi.org/10.1175/JCLI-D-17-0197.1

Deza M, Deza E (2016) Encyclopedia of distances, 4th edn. Springer, Heidelberg

Diks CGH, Vrugt JA (2010) Comparison of point forecast accuracy of model averaging methods in hydrologic applications. Stoch Environ Res Risk Assess 24(6):809–820. https://doi.org/10.1007/s00477-010-0378-z

Doblas-Reyes FJ, Hagedorn R, Palmer TN (2005) The rationale behind the success of multi-model ensembles in seasonal forecasting—II. Calibration and combination. Tellus A 57(3):234–252. https://doi.org/10.1111/j.1600-0870.2005.00104.x (**accessed 2018-07-24**)

Enemark T, Peeters LJ, Mallants D, Batelaan O, Valentine AP, Sambridge M (2019) Hydrogeological Bayesian hypothesis testing through trans-dimensional sampling of a stochastic water balance model. Water 11(7):1463. https://doi.org/10.3390/w11071463

Evans JP, Ji F, Abramowitz G, Ekström M (2013) Optimally choosing small ensemble members to produce robust climate simulations. Environ Res Lett 8(4):044050. https://doi.org/10.1088/1748-9326/8/4/044050

Ferré TPA (2017) Revisiting the relationship between data, models, and decision-making. Groundwater 55(5):604–614. https://doi.org/10.1111/gwat.12574

Fritsch JM (2000) Model Consensus. Weather Forecast 15:571–582

Garthwaite PH, Mubwandarikwa E (2010) Selection of weights for weighted model averaging: prior weights for weighted model averaging. Aust N Zeal J Stat 52(4):363–382. https://doi.org/10.1111/j.1467-842X.2010.00589.x

Gayler S, Wang E, Priesack E, Schaaf T, Maidl F-X (2002) Modeling biomass growth, N-uptake and phenological development of potato crop. Geoderma 105(3):367–383. https://doi.org/10.1016/S0016-7061(01)00113-6

Gayler S, Ingwersen J, Priesack E, Wöhling T, Wulfmeyer V, Streck T (2013) Assessing the relevance of subsurface processes for the simulation of evapotranspiration and soil moisture dynamics with CLM3.5: comparison with field data and crop model simulations. Environ Earth Sci 69(2):415–427. https://doi.org/10.1007/s12665-013-2309-z

Georgakakos KP, Seo D-J, Gupta H, Schaake J, Butts MB (2004) Towards the characterization of streamflow simulation uncertainty through multimodel ensembles. J Hydrol 298(1–4):222–241. https://doi.org/10.1016/j.jhydrol.2004.03.037

George EI (2010) Dilution priors: Compensating for model space redundancy. In: Institute of Mathematical Statistics Collections. Institute of Mathematical Statistics, Beachwood, Ohio, USA, pp 158–165. https://doi.org/10.1214/10-IMSCOLL611

Gneiting T, Raftery AE (2007) Strictly proper scoring rules, prediction, and estimation. J Am Stat Assoc 102(477):359–378. https://doi.org/10.1198/016214506000001437

Hagedorn R, Doblas-Reyes FJ, Palmer TN (2005) The rationale behind the success of multi-model ensembles in seasonal forecasting—I. Basic concept. Tellus A 57(3):219–233. https://doi.org/10.1111/j.1600-0870.2005.00103.x

Höge M, Guthke A, Nowak W (2019) The hydrologist's guide to Bayesian model selection, averaging and combination. J Hydrol 572:96–107. https://doi.org/10.1016/j.jhydrol.2019.01.072

Höge M, Guthke A, Nowak W (2020) Bayesian model weighting: the many faces of model averaging. Water 12(2):309. https://doi.org/10.3390/w12020309

Hutson JL, Wagenet RJ (1995) An Overview of LEACHM: A Process Based Model of Water and Solute Movement, Transformations, Plant Uptake and Chemical Reactions in the Unsaturated Zone. In: Loeppert RH, Schwab AP, Goldberg S (eds) Chemical equilibrium and reaction models. SSSA Special Publications, Soil Science Society of America and American Society of Agronomy, Madison, WI, USA, pp. 409–422. https://doi.org/10.2136/sssaspecpub42.c19

Jefferys WH, Berger JO (1992) Ockham's Razor and Bayesian analysis. American Scientist 80(1):64–72.http://www.jstor.org/stable/29774559

Johnsson H, Bergstrom L, Jansson P-E, Paustian K (1987) Simulated nitrogen dynamics and losses in a layered agricultural soil. Agric Ecosyst Environ 18(4):333–356. https://doi.org/10.1016/0167-8809(87)90099-5

Jones CA (1986) CERES-Maize; a simulation model of maize growth and development vol. 04; SB91. M2, J6

Knutti R, Sedláček J, Sanderson BM, Lorenz R, Fischer EM, Eyring V (2017) A climate model projection weighting scheme accounting for performance and interdependence: model projection weighting scheme. Geophys Res Lett. https://doi.org/10.1002/2016GL072012 (**accessed 2018-07-30**)

Krishnamurti TN, Kishtawal CM, Zhang Z, LaRow T, Bachiochi D, Williford E, Gadgil S, Surendran S (2000) Multimodel ensemble forecasts for weather and seasonal climate. J Clim

13(23):4196–4216. https://doi.org/10.1175/1520-0442(2000)0134196:MEFFWA2.0.CO;2 (**accessed 2018-07-24**)

Lever J, Krzywinski M, Altman N (2016) Model selection and overfitting. Nat Methods 13(9):703–704. https://doi.org/10.1038/nmeth.3968

Liu S, Maljovec D, Wang B, Bremer P-T, Pascucci V (2017) Visualizing high-dimensional data: advances in the past decade. IEEE Trans Vis Comput Graph 23(3):1249–1268. https://doi.org/10.1109/TVCG.2016.2640960

Makowski D (2017) A simple Bayesian method for adjusting ensemble of crop model outputs to yield observations. Eur J Agron 88:76–83. https://doi.org/10.1016/j.eja.2015.12.012

...Martre P, Wallach D, Asseng S, Ewert F, Jones JW, Rötter RP, Boote KJ, Ruane AC, Thorburn PJ, Cammarano D, Hatfield JL, Rosenzweig C, Aggarwal PK, Angulo C, Basso B, Bertuzzi P, Biernath C, Brisson N, Challinor AJ, Doltra J, Gayler S, Goldberg R, Grant RF, Heng L, Hooker J, Hunt LA, Ingwersen J, Izaurralde RC, Kersebaum KC, Müller C, Kumar SN, Nendel C, O'leary G, Olesen JE, Osborne TM, Palosuo T, Priesack E, Ripoche D, Semenov MA, Shcherbak I, Steduto P, Stöckle CO, Stratonovitch P, Streck T, Supit I, Tao F, Travasso M, Waha K, White JW, Wolf J (2015) Multimodel ensembles of wheat growth many models are better than one. Glob Change Biol 21(2):911–925. https://doi.org/10.1111/gcb.12768

Minka TP (2002) Bayesian model averaging is not model combination. Technical report

Nandi G, Sharma RK (2020) Data Science fundamentals and practical approaches: understand why data science is the next. BPB Publications, Delhi

Nearing GS, Gupta HV (2018) Ensembles vs. information theory: supporting science under uncertainty. Front Earth Sci 12(4):653–660. https://doi.org/10.1007/s11707-018-0709-9

Novoselova N, Wang J, Klawonn F (2015) Optimized leaf ordering with class labels for hierarchical clustering. J Bioinform Comput Biol 13(04):1550012. https://doi.org/10.1142/S0219720015500122

Palosuo T, Kersebaum KC, Angulo C, Hlavinka P, Moriondo M, Olesen JE, Patil RH, Ruget F, Rumbaur C, Takáč J, Trnka M, Bindi M, Çaldağ B, Ewert F, Ferrise R, Mirschel W, Şaylan L, Šiška B, Rötter R (2011) Simulation of winter wheat yield and its variability in different climates of Europe: a comparison of eight crop growth models. Eur J Agron 35(3):103–114. https://doi.org/10.1016/j.eja.2011.05.001

Priesack E (2006) Expert-N Dokumentation der Modellbibliothek: Zugl.: Göttingen, Univ., Habil.-Schr., 2006. FAM-Bericht, vol. 60. Hieronymus, München

Priesack E, Gayler S (2009) Agricultural crop models: concepts of resource acquisition and assimilate partitioning. In: Lüttge U, Beyschlag W, Büdel B, Francis D (eds) Progress in botany. Springer, Berlin, pp 195–222. https://doi.org/10.1007/978-3-540-68421-3_9

Rettie FM, Gayler S, Weber TKD, Tesfaye K, Streck T (2022) Climate change impact on wheat and maize growth in Ethiopia: a multi-model uncertainty analysis. PLoS One 17(1):1. https://doi.org/10.1371/journal.pone.0262951

Richards LA (1931) Capillary conduction of liquids through porous mediums. J Appl Phys 1(5):318–333

Richardson LF (1922) Weather prediction by numerical process. Cambridge University Press, Cambridge

Ritchie JT, Godwin D (1989) CERES Wheat 2.0. Publication Title: CERES Wheat 2.0

Ritchie JT, Godwin DC, Otter-Nacke S (1988) CERES-Wheat. A simulation model of wheat growth and development. University of Texas Press, Austin

Rizzo ML, Székely GJ (2016) Energy distance. Wiley Interdiscip Rev Comput Stat 8(1):27–38. https://doi.org/10.1002/wics.1375

Rosenzweig C, Jones JW, Hatfield JL, Ruane AC, Boote KJ, Thorburn P, Antle JM, Nelson GC, Porter C, Janssen S, Asseng S, Basso B, Ewert F, Wallach D, Baigorria G, Winter JM (2013) The Agricultural Model Intercomparison and Improvement Project (AgMIP): protocols and pilot studies. Agric For Meteorol 170:166–182. https://doi.org/10.1016/j.agrformet.2012.09.011

Sanderson BM, Knutti R, Caldwell P (2015) Addressing interdependency in a multimodel ensemble by interpolation of model properties. J Clim 28(13):5150–5170. https://doi.org/10.1175/JCLI-D-14-00361.1

Sanderson BM, Knutti R, Caldwell P (2015) A representative democracy to reduce interdependency in a multimodel ensemble. J Clim 28(13):5171–5194. https://doi.org/10.1175/JCLI-D-14-00362.1

Šmunek J, Huang K, van Genuchten MT (1998) The HYDRUS code for simulating the one-dimensional movement of water, heat, and multiple solutes in variably-saturated media, version 6.0: Research Report No. 144. U.S. Salinity Laboratory, Riverside, California

Spitters CJT, van Keulen H, van Kraalingen DWG (1989) A simple and universal crop growth simulator: SUCROS87. In: Rabbinge R, Ward SA, van Laar HH (eds) Simulation and systems management in crop protection. Simulation monographs. Pudoc, Wageningen, The Netherlands, pp 147–181

Streck T, Weber TKD (2020) Analytical expressions for noncapillary soil water retention based on popular capillary retention models. Vadose Zone J 19:e20042. https://doi.org/10.1002/vzj2.20042

Székely GJ, Rizzo ML (2013) Energy statistics: a class of statistics based on distances. J Stat Plan Infer 143(8):1249–1272. https://doi.org/10.1016/j.jspi.2013.03.018

Tebaldi C, Knutti R (2007) The use of the multi-model ensemble in probabilistic climate projections. Philos Trans R Soc A Math Phys Eng Sci 365(1857):2053–2075. https://doi.org/10.1098/rsta.2007.2076

van Dam JC, Groenendijk P, Hendriks RFA, Kroes JG (2008) Advances of modeling water flow in variably saturated soils with SWAP. Vadose Zone J 7(2):640. https://doi.org/10.2136/vzj2007.0060

van Genuchten MT (1980) Closed-form equation for predicting the hydraulic conductivity of unsaturated soils. Soil Sci Soc Am J 44(5):892–898

van Laar HH, Goudriaan J, Keulen H (1997) Sucros97: Simulation of Crop Growth for Potential and Water-limited Situations. Service Agricultural Sciences (DLO), Wageningen, The Netherlands. Backup Publisher: Res. Inst. for Agrobiol. and Soil-Fertility and The C.T. de Wit Graduate Schl. for Prod. Ecol

Van Laar H, Goudriaan J, Van Keulen H (1992) Simulation of crop growth for potential and water-limited production situations: as applied to spring wheat. Technical report, CABO-DLO

Vehtari A, Ojanen J (2012) A survey of Bayesian predictive methods for model assessment, selection and comparison. Stat Surv 6:142–228. https://doi.org/10.1214/12-SS102

Vogel RM, Sankarasubramanian A (2003) Validation of a watershed model without calibration. Water Resour Res. https://doi.org/10.1029/2002WR001940

Wallach D (2011) Crop model calibration: a statistical perspective. Agron J 103(4):1144–1151. https://doi.org/10.2134/agronj2010.0432

Wallach D, Martre P, Liu B, Asseng S, Ewert F, Thorburn PJ, van Ittersum M, Aggarwal PK, Ahmed M, Basso B, Biernath C, Cammarano D, Challinor AJ, De Sanctis G, Dumont B, Eyshi Rezaei E, Fereres E, Fitzgerald GJ, Gao Y, Garcia-Vila M, Gayler S, Girousse C, Hoogenboom G, Horan H, Izaurralde RC, Jones CD, Kassie BT, Kersebaum KC, Klein C, Koehler AK, Maiorano A, Minoli S, Müller C, Naresh Kumar S, Nendel C, O'Leary GJ, Palosuo T, Priesack E, Ripoche D, Rötter RP, Semenov MA, Stöckle C, Stratonovitch P, Streck T, Supit I, Tao F, Wolf J, Zhang Z (2018) Multi-model ensembles improve predictions of crop–environment–management interactions. Glob Change Biol. https://doi.org/10.1111/gcb.14411

Wallach D, Palosuo T, Thorburn P, Hochman Z, Gourdain E, Andrianasolo F, Asseng S, Basso B, Buis S, Crout N, Dibari C, Dumont B, Ferrise R, Gaiser T, Garcia C, Gayler S, Ghahramani A, Hiremath S, Hoek S, Horan H, Hoogenboom G, Huang M, Jabloun M, Jansson PE, Jing Q, Justes E, Kersebaum KC, Klosterhalfen A, Launay M, Lewan E, Luo Q, Maestrini B, Mielenz H, Moriondo M, Zadeh HN, Padovan G, Olesen JE, Poyda A, Priesack E, Pullens JWM, Qian B, Schütze N, Shelia V, Souissi A, Specka X, Srivastava AK, Stella T, Streck T, Trombi G, Wallor E, Wang J, Weber TKD, Weihermüller L, de Wit A, Wöhling T, Xiao L, Zhao C, Zhu Y, Seidel SJ (2020) The chaos in calibrating crop models. Plant Biol. https://doi.org/10.1101/2020.09.12.294744

Wang E (1997) Development of a generic process-oriented model for simulation of crop growth. Ökologie (Munich, Germany). Utz, Wissenschaft, Munich

Wang E, Engel T (1998) Simulation of phenological development of wheat crops. Agric Syst 58(1):1–24. https://doi.org/10.1016/S0308-521X(98)00028-6

Wang E, Engel T (2000) SPASS: a generic process-oriented crop model with versatile windows interfaces. Environ Model Softw 15(2):179–188. https://doi.org/10.1016/S1364-8152(99)00033-X

Weber TKD, Durner W, Streck T, Diamantopoulos E (2019) A modular framework for modelling unsaturated soil hydraulic properties over the full moisture range. Water Resour Res. https://doi.org/10.1029/2018WR024584

Weber TKD, Finkel M, Conceição Gonçalves M, Vereecken H, Diamantopoulos E (2020) Pedotransfer function for the Brunswick soil hydraulic property model and comparison to the van Genuchten-Mualem model. Water Resour Res. https://doi.org/10.1029/2019WR026820

Weber TKD, Ingwersen J, Högy P, Poyda A, Wizemann H-D, Demyan MS, Bohm K, Eshonkulov R, Gayler S, Kremer P, Laub M, Nkwain YF, Troost C, Witte I, Cadisch G, Müller T, Fangmeier A, Wulfmeyer V, Streck T (2021) Multi-site, multi-crop measurements in the soil-vegetation-atmosphere continuum: a comprehensive dataset from two climatically contrasting regions in South West Germany for the period 2009–2018. Earth Syst Sci Data Discuss 2021:1–32. https://doi.org/10.5194/essd-2020-396

Weigel AP, Liniger MA, Appenzeller C (2008) Can multi-model combination really enhance the prediction skill of probabilistic ensemble forecasts? Q J R Meteorol Soc 134(630):241–260. https://doi.org/10.1002/qj.210 (**accessed 2018-07-24**)

Winter CL, Nychka D (2010) Forecasting skill of model averages. Stoch Environ Res Risk Assess 24(5):633–638. https://doi.org/10.1007/s00477-009-0350-y

Wöhling T, Geiges A, Nowak W, Gayler S, Högy P, Wizemann HD (2013) Towards optimizing experiments for maximum-confidence model selection between different soil–plant models. Procedia Environ Sci 19:514–523. https://doi.org/10.1016/j.proenv.2013.06.058

Wöhling T, Schöniger A, Gayler S, Nowak W (2015) Bayesian model averaging to explore the worth of data for soil–plant model selection and prediction. Water Resour Res 51(4):2825–2846. https://doi.org/10.1002/2014WR016292

Xu R, Wunsch D (2008) Clustering. IEEE Press Series on Computational Intelligence. Wiley, New Jersey

Yao Y, Vehtari A, Simpson D, Gelman A (2018) Using stacking to average Bayesian predictive distributions (with discussion). Bayesian Anal 13(3):917–1007. https://doi.org/10.1214/17-BA1091

Yun K, Hsiao J, Jung M-P, Choi I-T, Glenn DM, Shim K-M, Kim S-H (2017) Can a multi-model ensemble improve phenology predictions for climate change studies? Ecol Model 362:54–64. https://doi.org/10.1016/j.ecolmodel.2017.08.003

Ziel F, Berk K (2019) Multivariate forecasting evaluation: on sensitive and strictly proper scoring rules. arXiv:1910.07325 [econ, stat]